

PREPARED FOR THE U.S. DEPARTMENT OF ENERGY,
UNDER CONTRACT DE-AC02-76CH03073

PPPL-3683
UC-70

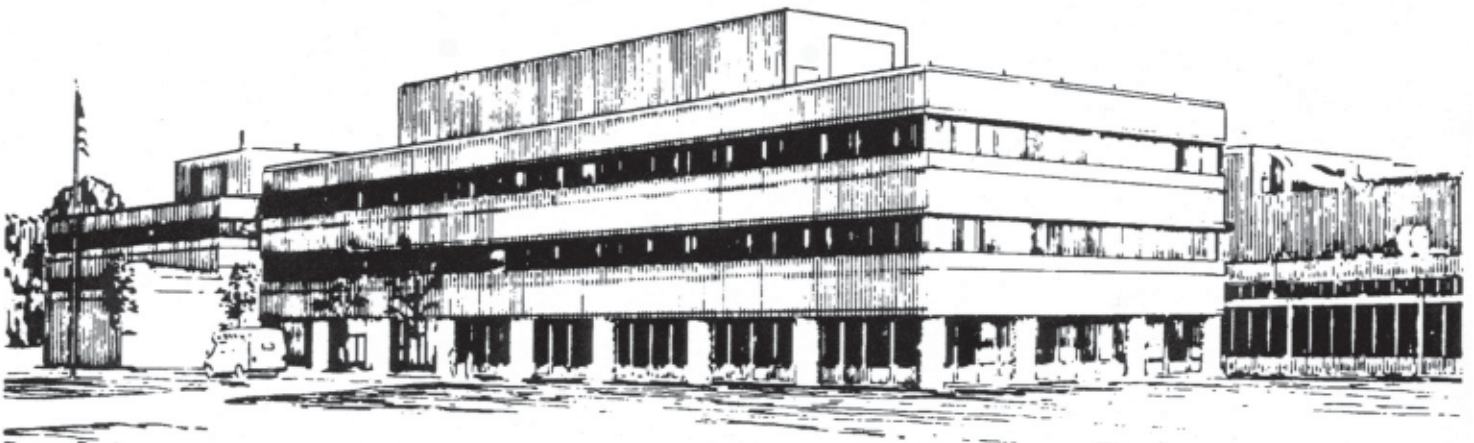
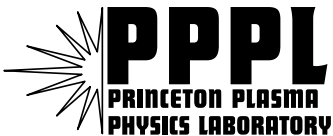
PPPL-3683

**Recent Advancements in Microwave Imaging
Plasma Diagnostics**

by

H. Park, C.C. Chang, B.H. Deng, C.W. Domier, A.J.H. Donné, K. Kawahata,
C. Liang, X.P. Liang, H.J. Lu, N.C. Luhmann, Jr., A. Mase, H. Matsuura,
E. Mazzucato, A. Miura, K. Mizuno, T. Munsat, K. and Y. Nagayama,
M.J. van de Pol, J. Wang, Z.G. Xia, and W-K. Zhang

March 2002



**PRINCETON PLASMA PHYSICS LABORATORY
PRINCETON UNIVERSITY, PRINCETON, NEW JERSEY**

PPPL Reports Disclaimer

This report was prepared as an account of work sponsored by an agency of the United States Government. Neither the United States Government nor any agency thereof, nor any of their employees, makes any warranty, express or implied, or assumes any legal liability or responsibility for the accuracy, completeness, or usefulness of any information, apparatus, product, or process disclosed, or represents that its use would not infringe privately owned rights. Reference herein to any specific commercial product, process, or service by trade name, trademark, manufacturer, or otherwise, does not necessarily constitute or imply its endorsement, recommendation, or favoring by the United States Government or any agency thereof. The views and opinions of authors expressed herein do not necessarily state or reflect those of the United States Government or any agency thereof.

Availability

This report is posted on the U.S. Department of Energy's Princeton Plasma Physics Laboratory Publications and Reports web site in Fiscal Year 2002. The home page for PPPL Reports and Publications is: http://www.pppl.gov/pub_report/

DOE and DOE Contractors can obtain copies of this report from:

U.S. Department of Energy
Office of Scientific and Technical Information
DOE Technical Information Services (DTIS)
P.O. Box 62
Oak Ridge, TN 37831

Telephone: (865) 576-8401

Fax: (865) 576-5728

Email: reports@adonis.osti.gov

This report is available to the general public from:

National Technical Information Service
U.S. Department of Commerce
5285 Port Royal Road
Springfield, VA 22161

Telephone: 1-800-553-6847 or
(703) 605-6000

Fax: (703) 321-8547

Internet: <http://www.ntis.gov/ordering.htm>

RECENT ADVANCEMENTS IN MICROWAVE IMAGING PLASMA DIAGNOSTICS

H. Park¹, C.C. Chang², B.H. Deng², C.W. Domier², A.J.H. Donné³, K. Kawahata⁴, C. Liang², X.P. Liang², H.J. Lu², N.C. Luhmann, Jr.², A. Mase⁵, H. Matsuura⁶, E. Mazzucato¹, A. Miura⁶, K. Mizuno⁷, T. Munsat¹, K. and Y. Nagayama⁴, M.J. van de Pol³, J. Wang², and Z.G. Xia², W-K. Zhang²

ABSTRACT

Significant advances in microwave and millimeter wave technology over the past decade have enabled the development of a new generation of imaging diagnostics for current and envisioned magnetic fusion devices. Prominent among these are revolutionary microwave electron cyclotron emission imaging (ECEI), microwave phase imaging interferometers, imaging microwave scattering and microwave imaging reflectometer (MIR) systems for imaging T_e and n_e fluctuations (both turbulent and coherent) and profiles (including transport barriers) on toroidal devices such as tokamaks, spherical tori and stellarators. The diagnostic technology is reviewed, and typical diagnostic systems are analyzed. Representative experimental results obtained with these novel diagnostic systems are also presented.

-
1. Plasma Physics Laboratory, Princeton University, Princeton, New Jersey 08543, U.S.A.
 2. Department of Applied Science, University of California at Davis, Davis, California 95616, U.S.A.
 3. FOM-Instituut voor Plasmafysica Rijnhuizen, Associatie EURATOM-FOM, Trilateral Euregio Cluster, 3430 BE, Nieuwegein, The Netherlands
 4. National Institute for Fusion Science, Toki 509-5292, Japan
 5. Advanced Science and Technology Center for Cooperative Research, Kyushu University Kasuga 816-8580, Japan
 6. Development Project Center, Corporate R & D Center, Yokogawa Electric Corporation, Musashino 180-8750, Japan
 7. Research Institute of Electrical Communication, Tohoku University, Sendai 980-0812, Japan

1. INTRODUCTION

The problem of anomalous transport in magnetized plasmas and its relationship to small amplitude microturbulence continues to be of critical importance to a basic physics understanding as well as the eventual realization of magnetic fusion energy. Recently, significant experimental progress has been made in suppressing microturbulence in either the plasma edge, some internal regions, or both to form transport barriers, thereby achieving various high confinement modes of operation. Also, theoretical understanding of plasma turbulence and anomalous transport has been greatly enriched with the help of the rapid advancement of computer technology, which, for example, has made it possible in extensive computer simulations to reveal elegant three-dimensional (3-D) structures of plasma turbulence¹⁻⁴. However, the behavior of the turbulence process(es) remains poorly understood experimentally, which prevents the advent of efficient means of turbulence suppression and improvement of plasma confinement. This is primarily due to the difficulty in diagnosing the small amplitude fluctuations in the high temperature plasma core⁵. Among the equally important fluctuation quantities of plasma density ($\tilde{n}_{e,i}$), temperature ($\tilde{T}_{e,i}$), potential ($\tilde{\phi}$), and magnetic field (\tilde{B}), \tilde{n}_e was the only fluctuation quantity that had been extensively diagnosed by various techniques, including microwave and far infrared scattering, probes, reflectometry, phase contrast imaging, and heavy ion beam probes. Information regarding \tilde{T}_e in the plasma core region was not available until the introduction of intensity interferometric techniques into the ECE diagnostic in 1993⁶. More importantly, plasma turbulence imaging diagnostics were not available until quite recently, and are currently still in an early stage of development. Furthermore, quantitative analysis of the limitations^{7,8} in conventional reflectometry supported by experiments has guided

us to develop an imaging system based on reflectometry. Therefore, it is not surprising to learn that it has been impossible to verify or reject the predictions of computer simulations based on the limited experimental data. Of equal importance is the need for detailed study of plasma filamentation and the formation of internal transport barriers, which often appear to have fine scale structures in profiles, and therefore require high spatial and temporal resolution measurements⁹. Numerous studies have stressed the need for high resolution imaging diagnostics, which will ultimately permit the visualization of these complicated 2-D and 3-D structures of both electron temperature and density.

Fortunately, the combination of the applicability of the microwave/millimeter wave portion of the spectrum to several important plasma diagnostic techniques (scattering, reflectometry, electron cyclotron emission/absorption, and interferometry/polarimetry) together with recent revolutionary advances in microwave technology have made this possible for the first time. The general principles of the above diagnostic techniques can be found in a number of references^{5, 10-14}. The focus and emphasis of this paper will therefore primarily be on the dramatic breakthroughs which are occurring in electron cyclotron emission imaging (ECEI), microwave imaging reflectometry (MIR), and imaging interferometry together with the emerging technique of cross-polarization scattering and imaging microwave scattering.

2. ELECTRON CYCLOTRON EMISSION IMAGING (ECEI)

In magnetized plasmas, the gyro motion of electrons results in plasma radiation at the electron cyclotron frequency $\omega_{ce} = eB/m_e$ and its harmonics. Here, B is the magnetic field strength, e is the electron charge, and m_e is the kinetic electron mass. When the plasma density

and temperature are sufficiently high, the plasma becomes optically thick to some harmonics of the electron cyclotron emission (ECE), usually, the first harmonic ordinary mode and the second harmonic extraordinary mode^{13,15}. The radiation intensity of optically thick ECE harmonics reaches that of black body radiation, i.e.,

$$I(\omega) = \omega^2 T_e / (8\pi^3 c^2) \quad (1)$$

Therefore, the plasma electron temperature and its fluctuations can be diagnosed by measuring the intensity of ECE.

For contemporary magnetic fusion devices such as tokamaks, the magnetic field is several Tesla, so that the ECE radiation is in the millimeter wave range. The typical range of frequencies for second harmonic ECE radiation is shown in Fig. 1, which is a plot of the characteristic frequencies for the TEXTOR-94 device. This is seen to cover the range of *100-150 GHz* or the so-called W- and D- waveguide bands. It is noted that the ECE frequency is a monotonically decreasing function of plasma radius towards the outboard side, originating from the magnetic configuration of tokamaks, in which the magnetic field strength depends on the plasma minor radius as

$$B(r) = B_0 R_0 / (R_0 + r) \quad (2)$$

where R_0 and r are the major radius and minor radius of the tokamak, respectively. In a conventional ECE radiometer, a horn antenna receives the ECE radiation at the out board side, which is separated into different frequency bands, each corresponding to a different horizontal location in the plasma. Thus, time resolved 1-D T_e profiles can be obtained.

An ECE radiometer has a resolution limit due to the intrinsic radiation noise given by Ref. 16

$$\Delta T_{rms} = (T_e + T_n) / \sqrt{\Delta\omega\tau} \quad (3)$$

where T_e is the electron temperature to be measured, T_n ($\ll T_e$) is the system noise temperature, $\Delta\omega$ is the bandwidth of the radiation to be collected, and τ is the integration time. For a typical ECE radiometer, the bandwidth is designed to be around 0.5 GHz based on spatial resolution considerations; thus, the relative temperature resolution limit is about 1-3% with a frequency response of 250 kHz . As the relative fluctuation amplitude of microturbulence is typically $< 1\%$, the intrinsic radiation noise of an ECE radiometer usually predominates.

Despite the above, the spectra as well as the root-mean-square (rms) values of turbulent T_e fluctuations can be measured by applying intensity interferometric techniques to the ECE signals^{6, 17-26}. The key is to obtain two signals that have uncorrelated radiation noise, so that the cross coherence of the two signals is¹⁸

$$\begin{aligned} \Gamma_{12}(\tau) &= \overline{\tilde{S}_1(t)\tilde{S}_2(t+\tau)} \\ &= c_1 c_2 \overline{(\tilde{T}_{e1} + \bar{T}_{e1}\tilde{N}_1)(\tilde{T}_{e2} + \bar{T}_{e2}\tilde{N}_2)} \\ &= c_1 c_2 \left(\overline{\tilde{T}_{e1}\tilde{T}_{e2}} + \overline{\bar{T}_{e1}\tilde{T}_{e2}\tilde{N}_1} + \overline{\tilde{T}_{e1}\bar{T}_{e2}\tilde{N}_2} + \overline{\bar{T}_{e1}\bar{T}_{e2}\tilde{N}_1\tilde{N}_2} \right) \\ &\approx c_1 c_2 \left(\overline{\tilde{T}_{e1}\tilde{T}_{e2}} + \overline{\bar{T}_{e1}\bar{T}_{e2}\tilde{N}_1\tilde{N}_2} \right) \\ &= c_1 c_2 \overline{\tilde{T}_{e1}(t)\tilde{T}_{e2}(t+\tau)} \end{aligned} \quad (4)$$

Here, c_1 and c_2 are constant sensitivity coefficients of the detection system channels. If the two signals are from the same plasma volume, $T_{e1} = T_{e2}$, so that local values of \tilde{T}_e can be obtained. If the two signals are from poloidally or radially separated plasma volumes, the poloidal or radial

wavenumber spectra and correlation lengths can be measured. A variety of intensity interferometric techniques are reviewed in Ref. 19, and will not be discussed in detail in this review. The particular techniques utilized in our ECE imaging diagnostics will be described briefly later in this section.

The need for the first ECE imaging diagnostic was clearly demonstrated through experiments on the TEXT-U tokamak. When the first \tilde{T}_e data from the plasma core were available, it was found that critical information such as the poloidal wavenumber and correlation length could not be obtained using conventional ECE radiometers. In addition, the relatively poor spatial resolution of conventional ECE has limited its sensitive wavenumber spectral range due to sample volume effects^{17,18,27}. These problems were solved when the high spatial resolution ECE imaging diagnostic was developed and implemented on TEXT-U, which measured the poloidal wavenumbers, statistical dispersion relations, and poloidal correlation lengths of electron temperature fluctuations in the plasma core for the first time^{23,28}. An ECEI system was subsequently developed for the RTP tokamak²⁹, and more recently implemented on TEXTOR-94³⁰. ECE imaging systems have now also been developed and installed on mirror machines and stellarators^{31,32}. Shown in Fig. 2 is a schematic diagram outlining the principle of ECE imaging. Second harmonic, extraordinary mode electron cyclotron radiation is collected and imaged onto a mixer/receiver array comprised of planar antennas with integrated Schottky diodes. This arrangement has the advantages of wide radio frequency (RF) and intermediate frequency (IF) bandwidths, ease of fabrication, and low cost. The elements of the array are aligned along the \mathbf{E} field (vertical) direction to collect second harmonic X-mode radiation. In the Imaging Array Development section of this review, a variety of possible implementations are described. An array of sample volumes in the plasma, aligned along the vertical direction, is imaged onto the

array. In the case of a tokamak plasma, there is a one-to-one mapping of the electron cyclotron frequency to the major radius due to the monotonic variation of the magnetic field (Eq. 2). This allows the ECEI focal plane to be swept through the plasma by sweeping the receiver frequency of the array. Using a 1-D detector array, one is then able to obtain 2-D images of the electron temperature profile over the minor plasma cross section. The ECEI system as configured for the initial RTP tests is shown in Fig. 3. The system shared the same port as the Thomson scattering system thereby providing a convenient calibration check. In the various ECEI systems, the sample volumes were essentially 1.2 cm cubes (diameters at $1/e$ power) and were capable of resolving temperature fluctuations with a wavenumber range of $k < 2.8\text{ cm}^{-1}$ ²⁶.

As noted above, high-resolution measurement of profiles is critical for the understanding of the physics of plasma filamentation and the formation of internal transport barriers to name just two examples²⁵. Figure 4 is a representative high spatial resolution measurement of T_e profiles in the RTP tokamak. During off-axis ECRH, an $m=2$ mode is observed to be localized at the sawtooth inversion radius ($r \sim 3.5\text{ cm}$), with a radial extent of less than 2 cm . This mode is very stable, and can survive the sawtooth crashes. Figures 5 and 6 illustrate initial ECEI data obtained on TEXTOR-94 in tests of the prototype version of the instrument.

As discussed above, turbulent temperature fluctuations are measured with ECEI using the technique of intensity interferometry^{6, 17-26}. The key issue is to obtain two signals, which have uncorrelated thermal fluctuations, or radiation noise. This decorrelated intrinsic noise can then be averaged out in statistical analysis to reveal the usually smaller plasma T_e fluctuations due to plasma instabilities, as the latter have different coherence properties from the thermal fluctuations. One of the techniques is illustrated in Fig. 7. Due to the natural line width of ECE

radiation¹³, each frequency band corresponds to an extended plasma volume thickness along the measurement sight line. When the frequency bands are close to each other, the plasma volumes will be mostly overlapped, with their separation much less than the correlation length of turbulent fluctuations. Therefore, the two resultant signals have essentially the same temperature fluctuation. However, once the filters have sufficient isolation, i.e., more than -20 dB at the cross point, the radiation noise of the two signals are uncorrelated¹⁷. The cross correlation between the two signals then yields the local values of the temperature fluctuations¹⁷⁻³³. Another technique is illustrated in Fig. 8. Because distinct plasma volumes have uncorrelated radiation noise, the signals from two such volumes can be cross-correlated (provided their separation is not too much larger than the fluctuation correlation length) to determine the wave dispersive properties. Shown in Fig. 9 is an example of the cross power spectral density and the statistical dispersion relation of T_e fluctuations measured by the ECEI system in RTP²⁵. Usually, two modes can be identified in the fluctuation spectra. The low frequency mode is attributed to MHD activity, while the high frequency mode has wider bandwidth and is attributed to turbulent fluctuations. In this example, the turbulent mode is propagating in the ion diamagnetic drift direction, and is believed to be due to the ion temperature gradient instability²⁵. Another example is shown in Fig. 10, which is a 2D image of the fluctuation amplitude, measured on a shot to shot basis in RTP²⁵. It is seen that turbulence is not uniformly distributed over the plasma cross-section. Instead, prominent peaks are seen in the plasma confinement region, which may be related to the coherent structures predicted by theory^{34,35}. Of particular interest are the peaks of both MHD and turbulence in the tokamak midplane, outside the $q = 2$ radius, in both the high and low field side^{24,25,35}. This experimental finding is not expected from current theory.

In the ECEI system under development for TEXTOR-94, a multi-frequency heterodyne receiver is constructed for each of the imaging channels, so that 2-D maps of T_e profiles and fluctuations can be obtained in a single discharge, unlike the previous 1-D systems implemented on TEXT-U and RTP, in which successive discharges with varying toroidal B -field conditions or LO frequency were required²⁶. This new ECEI diagnostic represents a breakthrough in 2-D electron temperature profile and fluctuation measurements. For the study of \tilde{T}_e turbulence, the instrument makes it possible to simultaneously and unambiguously measure k_r and k_θ , which is essential for mode identification. In the case of T_e profiles and coherent mode phenomena such as MHD and sawteeth, this will allow direct observation of island/filament rotation without the assumption of rigid body rotation. The 2-D mapping also makes it considerably easier to overlap with MIR sample volumes for correlation studies between \tilde{T}_e and \tilde{n}_e fluctuations.

More recently, an ECEI instrument has been developed for use on the large helical device (LHD) at the National Institute for Fusion Science (NIFS) in Japan^{31,32}. The frequency of the second-harmonic ECE on LHD ranges from 120 GHz to 180 GHz . In order to cover this frequency range, a novel detector array using monolithic microwave integrated circuit (MMIC) technology was designed and fabricated and is described in the technology section of this paper.

Figures 11 and 12 show the schematic of the experimental arrangement. An ellipsoidal mirror and a plane mirror located inside the vacuum vessel converge the ECE signals to pass through a 192 mm diameter fused-quartz vacuum window. The signals are subsequently imaged onto a detector array. An object plane located at the plasma center is 2.7 m in front of the ellipsoidal mirror. The Airy pattern of a point source is measured in order to confirm the performance of the optical system along the x and y-axes. Here, a 140 GHz source is located at the position

Invited Review Article: Review of Scientific Instruments, 2002

corresponding to the plasma center and the source is imaged onto the detector array. The Airy patterns in the horizontal and vertical planes are shown in Fig. 13. The results are in good agreement with the theoretical values. The magnification of the optical system was also investigated experimentally and agrees well with the design value of 0.68. The ECE imaging system as shown in Fig. 11 is attached to the diagnostic port of LHD. The detector array is installed inside an aluminum box for electrical shielding, and a pyramidal horn antenna array in the TE_{10} mode is attached to the both sides of the detector array. The second-harmonic ECE signals in the extraordinary mode are mixed with the LO power on the detector array where the LO beam is focused onto the detectors by using a cylindrical lens. Figure 14 shows the IF system of the heterodyne receiver. The IF signals are amplified by a chain of amplifiers ($1-8$ GHz, 80 dB) and subsequently separated into 4-8 channels. Each signal is then band pass filtered. A range of filters is available with center frequency from 1 to 8 GHz at 1 GHz intervals; each has a 3 dB bandwidth of 300 MHz. The signals are then passed through square-law detectors.

The actual ECEI experiments on LHD began in 2001. The time evolutions of the signal output of each IF channel ($4-7$ GHz) are shown in Fig. 15. During the period $t=1.5-1.8$ s, ECRH power at 164 GHz is applied. The signal level after the ECRH pulse corresponds to the bulk electron temperature of the LHD plasma. The wideband characteristics of the detectors are quite convenient for the application of correlation radiometry as well as the measurement of broadband spectrum with fixed LO frequency.

3. MICROWAVE IMAGING REFLECTOMETRY (MIR)

Microwave reflectometry is a radar technique used to infer the electron density characteristics by probing the density-dependent cutoff layer in a magnetized plasma³⁶. Referring

to Fig. 1, an electromagnetic wave propagating through a magnetized plasma is reflected from a cutoff surface described by one of the three following conditions depending upon its polarization:

$$\omega = \omega_{pe} \quad (\text{Ordinary mode}) \quad (5)$$

$$\omega = \sqrt{\left(\frac{\omega_{ce}}{2}\right)^2 + \omega_{pe}^2} \pm \frac{\omega_{ce}}{2} \quad (\text{R and L extraordinary mode}) \quad (6)$$

where $\omega_{pe} = \sqrt{\frac{n_e e^2}{\epsilon_o m_e}}$.

The phase difference between the launched and reflected wave (traveling in the r direction and measured at the plasma edge) is given by $\phi = 2k_0 \int_0^{r_c} \sqrt{\epsilon} dr$ (apart from an additive constant) where k_0 is the free-space wavenumber of the probing wave, $\epsilon = (ck/\omega)^2$ is the plasma permittivity, and r_c is the position of the wave cutoff. Measurement of ϕ thus determines the location of r_c . By sweeping the frequency of the probing wave and recording the phase history from the beginning of the plasma discharge, the electron density profile can be determined (or the B-field for the case of X-mode if the density is known).

Since its first use for the investigation of low frequency microturbulence in tokamak plasmas^{37,38}, microwave reflectometry has become widely used for density profile and fluctuation measurements as well as magnetic field investigation^{36,39-46}. In the presence of density fluctuations, the reflected electromagnetic wave spectrum is broadened with a strong

weighting by those fluctuations in the vicinity of the cutoff layer. In the simplest case of small amplitude fluctuations and a 1-D plane stratified plasma permittivity, $\varepsilon = \varepsilon_0(r) + \tilde{\varepsilon}(r)$, with $\tilde{\varepsilon}(r) \ll 1$, the fluctuating component of the measured phase is given by the 1-dimensional geometric optics approximation⁷

$$\tilde{\phi} = k_0 \int_0^{r_c} \frac{\tilde{\varepsilon}(r)}{\sqrt{\varepsilon_0(r)}} dr, \quad (7)$$

and the power spectrum of the reflected phase fluctuations is related to that of the density fluctuations by Ref. 7

$$\Gamma_\phi(k_r) = \pi M k_0^2 L_n \Gamma_n(k_r) / |k_r| \quad (8)$$

In the above, $L_n = n / (dn/dr)_{r=r_c}$ is the density scale length, $M \equiv (n \partial E / \partial n)_{r=r_c}$, and it was assumed that $k_r < k_0 / (k_0 L_\varepsilon)^{1/3}$ where $L_\varepsilon = (d\varepsilon_0/dr)_{r=r_c}^{-1}$.

It is important to point out that the fluctuating phase of the reflected wave is dominated by the change in permittivity close to the cutoff layer, due to the factor $1/\sqrt{\varepsilon_0(r)}$ in the integral, which becomes very large near the cutoff (as the group velocity approaches zero). The measurement of fluctuating phase therefore represents a localized measurement of fluctuations near the cutoff layer, rather than a combined measurement of modulations along the entire ray trajectory. Indeed, this is one of the most valuable features of reflectometry as a fluctuation diagnostic.

In standard electron density fluctuation measurements with microwave reflectometry, the

probing wave is launched and received on the equatorial plane using a pair of small antennas. The measurement is essentially a point measurement, and does not provide direct information on the spatial structure of density fluctuations. A significant improvement in the capability of this technique is the method of correlation reflectometry, where the radial structure of plasma fluctuations is inferred from waves reflected from closely spaced cutoff layers.

The above 1-D geometrical optics approximation unfortunately breaks down in the case of multidimensional turbulent fluctuations, which is precisely the case of interest for magnetic fusion plasma diagnostics where there are large radial and poloidal variations. The need for Microwave Imaging Reflectometry (MIR) has been well documented through detailed reflectometry studies by Mazzucato, which have revealed the crucial need for reflectometric imaging (together with the failure of standard fluctuation reflectometry)⁷. The difference between standard 1-D reflectometry and 2-D is readily apparent from Fig. 16 below. It is seen that with 1-D fluctuations, the reflection layer will move back and forth in the radial direction, resulting in the phase changes in the reflected wave; with 2-D fluctuations, the backward field contains components from multiple fragmented wavefronts, resulting in a complicated interference pattern at the detector plane. This interference results in both amplitude and phase modulations in the detected signal, leading to a breakdown of the simple relationship between phase fluctuations and density fluctuations (Eq. 8). This was experimentally demonstrated on TFTR where the in-phase and quadrature reflectometer components were shown to behave as two independent variables with zero mean, as illustrated in Fig. 17⁷. Detailed numerical studies by Mazzucato verified this interpretation and also revealed that information of density fluctuations can be retrieved from data of specially designed imaging reflectometers, where the virtual reflecting cutoff layer is imaged onto the detector plane^{7,47}.

In the numerical study in Ref. 7, a plane-stratified plasma is perturbed by a wide spectrum of two-dimensional fluctuations with random phases. The phase of the reflected wave was simulated using a range of fluctuation amplitudes and spectral widths, and the results showed (as observed experimentally) that large fluctuations cause large amplitude modulations and random phases in the reflected wave, exhibiting predictable statistical behavior of both phase and amplitude. Figure 18 is an isometric surface plot of the normalized field amplitude of the return waves, as a function of r and x (radial and poloidal directions) for a case with fluctuations above the threshold for failure of the 1-D approximation. In the figure, r_b represents the plasma boundary and r_c represents the wave cutoff location. It illustrates the large random perturbation of the reflected wave amplitude away from the reflecting cutoff layer ($r > r_c$). The basic problem in extracting useful phase information from standard reflectometry data is that the measurements are usually performed at a large distance ($r > r_b$) from the reflecting layer where (in the absence of optical imaging) the reflected wavefront is scrambled (Fig. 18). As a result, what is sampled is a complicated interference pattern, with characteristics that may be completely different from those of the actual plasma fluctuations under investigation.

The most significant result of the numerical simulation studies was the demonstration of a “virtual cutoff” surface, located behind the actual cutoff surface, from which return waves appear to have reflected (to an observer at the plasma edge)⁷. This is shown in Fig.18 at $r = r_{min}$, where the modulation to the reflected wave amplitude is minimum. It is also shown in Ref. 7 that density fluctuations can be recovered from the phase changes of the reflected wave at the “virtual cutoff” ($r = r_{min}$), located behind the actual cutoff layer ($r = r_c$). Therefore, it is of crucial importance to use imaging optics to map the “virtual cutoff” layer onto the detector plane.

The location of the virtual cutoff can be heuristically described as the intersection of the asymptotes of the ray trajectories of the probing wave before and after reflection, shown schematically in Fig.19. Because of finite refraction due to the plasma near the cutoff, the trajectory of the probing wave is curved, with a radial turning point occurring at the cutoff layer. To an observer (or optical system) located at the plasma boundary, however, the wave appears to have reflected from a surface somewhat behind the actual cutoff.

If the reflected rays are collected by a large-aperture optical system, the spatial structure of the density fluctuations near the cutoff layer can be determined by a reconstruction of the reflected wavefront at the image plane; phase fluctuations measured at the image plane will directly correspond to density fluctuations at the cutoff layer. Additionally, the use of imaging optics enables the simultaneous sampling of an extended region of the cutoff layer by an extended array of detectors at the image plane. It is important to reiterate that the use of imaging optics extends the region of validity for reflectometry as a fluctuation diagnostic even for a single detector corresponding to a small probing beam. The use of multiple detectors to measure an extended plasma layer is a secondary benefit of the presence of imaging optics.

It was shown in Ref. 7 that for slab geometry, the virtual cutoff is located at a distance $\int_{r_c}^{r_b} \frac{1}{\sqrt{\epsilon_0(r)}} dr$ from the plasma boundary. Additionally, it was shown that the use of imaging optics provided an increased threshold below which phase fluctuation measurements could be directly correlated to density fluctuations. This condition is given (for ordinary-mode propagation) by $\sigma_n^2 < 1/(\pi^{3/2} L_n^2 \Delta k_x^2)$ where σ_n is the variance of the density fluctuations, L_n is the density scale-length, and Δk_x is the width of the poloidal fluctuations. For TFTR-like

parameters of $\Delta k_x = 0.5 \text{ cm}^{-1}$, $L_n = 50 \text{ cm}$, this breakdown occurs at $\sigma_n = 1.7 \times 10^{-2}$. It has subsequently been shown in Ref. 47 that the poloidal curvature of the plasma can reduce the physical separation between the virtual and actual cutoff layers, and can also increase the fluctuation thresholds for validity of both the 1-D geometrical optics approximation and the 2-D imaging optics criteria.

To summarize the above, in standard reflectometry the reflected waves from a “corrugated” cutoff layer interfere at the detector, causing both amplitude and phase modulation (see Fig. 20). Hence, the measured phase no longer directly corresponds to the density fluctuation. Fortunately, the use of imaging optics can solve this problem.

Shown in Fig. 21a is a schematic diagram outlining the experimental realization of reflectometric imaging based on the ECEI system shown in Fig. 3. First, a broad area of the plasma cutoff layer is illuminated by a millimeter-wave source. Focusing optics are utilized to transform the output of the illuminating source (typically a solid state oscillator) into an extended beam whose curved wavefront is designed to roughly match the poloidal/toroidal shape of the plasma cutoff surfaces. This wavefront curvature matching enhances the amplitude of the reflected waves, and ensures that a sufficient fraction of the incident electromagnetic power is coupled to the MIR receiver for detection. The reflected radiation passes back through the same imaging optics as the illuminating beam, with additional optics utilized to image the reflecting layer onto the imaging array. A second millimeter-wave source provides LO power to the imaging array, yielding output signals whose frequency is that of the difference frequency between the two sources. A quadrature detection system yields the fluctuating phase and amplitude signals on each array element. Unlike the ECEI system, the MIR system requires a

Invited Review Article: Review of Scientific Instruments, 2002

relatively powerful probing beam to be launched through the optical system while the expected signal level at the array coming from plasma reflections is relatively small. Unfortunately, standing wave problems arising from the multiple reflective lens surfaces forced a redesign of the system based on reflective optics. In this design, the primary optical elements consist of two large reflective focusing mirrors (toroidal and poloidal). Figure 21b is a 3-D AutoCAD design of the system briefly implemented and tested in TEXTOR-94.

Proof-of-principle experiments employing the systems shown in Figs. 21a and 21b, have been performed on the TEXTOR-94 tokamak using fixed-frequency versions of both the ECE and reflectometer subsystems, confirming the feasibility of the imaging scheme. One of the most significant results from the prototype MIR system is the demonstration of the virtual cutoff surface. In this experiment, both the probing frequency and the focal plane of the optics were held fixed, and the electron density was ramped over the course of the shot to bring the cutoff surface through and beyond the focal plane of the optics. Figure 22 shows the complex signal recorded over several 3 ms duration time windows as the cutoff surface moves outward through and beyond the optical focal plane. Both the characteristic crescent-shaped phase modulation when the cutoff is in-focus and the fill-in of the complex plot as the cutoff moves out of focus are clearly identifiable.

The two conceptual tests on TEXTOR-94 have revealed the critical importance of the probe beam quality, and have inspired us to examine the details of the formation and propagation of large Gaussian beams from the illumination source, as well as the performance of the optical elements. Many launching schemes for the source have been tested for the required phase fronts (no interference) and profiles (side lobes less than 25 dB). The profiles of the source beam at

various test stages are illustrated in Fig. 23. Beam profiles were produced from specialized launching antennas, and have been demonstrated to propagate cleanly through multiple optical components. The curvatures of the large reflective elements have been verified with a sophisticated alignment scheme using visible lasers. In the figure, 1-D “slices” in both the x and y direction (Figs. 23b, 23c) are shown next to the measured far-field 2-D beam pattern of the special horn (Fig. 23a). Here, squares represent single-point measurements, and solid lines represent the best-fit Gaussian profile. In Fig. 23d, squares represent measured beam widths, and the solid line represents the theoretical calculation of the Gaussian beam width propagating through the optical test system.

In addition to the detailed component tests, we have embarked on a comprehensive study to demonstrate the capabilities and limitations of the MIR technique, both theoretically and experimentally. Simultaneously with the installation of an improved TEXTOR instrument, we have initiated a systematic off-line laboratory study of reflectometry systems, using corrugated reflecting targets of known shape to simulate the fluctuating plasma reflection layer. A schematic of the MIR laboratory setup is shown in Fig. 24. Each reflecting target was tested using both the MIR configuration (Fig. 24) and a standard 1-D configuration (not shown) consisting of a launched Gaussian beam and a receiving horn with no optics. As a reference, each surface was independently measured using a visible-laser interferometer (Leica “Laser Tracker”). This approach was chosen to augment the plasma measurements due to the unavoidable complexity of any new plasma data; calibration of any new instrument is made much more reliable by first using known reference targets.

A result from this off-line study is shown in Fig. 25, in which both the MIR and 1-D instruments were used to reconstruct the phase of a target mirror with corrugations of $k_{\theta} = 1.25$

Invited Review Article: Review of Scientific Instruments, 2002

cm^{-1} . Figure 25a compares data from the 1-D configuration (located 30 cm from the target surface) to the reference measurement, and Fig. 25b compares data from the MIR instrument (located 235 cm from the target surface) to the reference measurement. Clearly from the plots, the MIR system faithfully reproduces the target fluctuations (at a distance of over 200 cm) while the conventional reflectometer data becomes completely distorted, even at a distance of 30 cm . This simple experiment demonstrates both the difficulties of interpreting conventional reflectometry data and the solutions offered by MIR techniques.

In order to quantify the degree to which the reflectometer measurements accurately reproduce the shape of the reference surface, the cross-correlation was calculated between the power spectra produced by the two reflectometers and the reference curves. Cross-correlation figures were calculated for measurements taken over a wide range of d , the distance between the instrument and the target surface. This data, plotted for both the 1-D and MIR systems, is shown in Fig. 25c.

For the 1-d case, the correlation is nearly unity for $d \sim 10\text{ cm}$, and falls to $\sim 40\%$ as the distance is increased to 30 cm or more. For the MIR system, there is near-unity correlation between the signal and reference curves everywhere within $\pm 10\text{ cm}$ of the focal distance, with a fairly sharp falloff as the image becomes unfocused, and the recorded phase begins to exhibit “phase runaway”. The strong correlation over this 20 cm range represents the distance over which multi-radial (multi-frequency) data could be collected simultaneously with a fixed set of imaging optics. Importantly, this data is taken with the instrument at a distance of over 200 cm from the reflecting surface, in exactly the configuration used for TEXTOR measurements. The region

$d < 50$ cm is shaded in Fig. 25c to represent the region inaccessible to diagnostic instruments for core measurements (i.e. $a = 46$ cm in TEXTOR, $a = 56$ cm in DIII-D, etc.).

It is important to note that this off-line test represents a simplified model of reflectometry of plasma fluctuations. Specifically, the target mirrors do not refract the waves in the vicinity of the reflecting surface, and have thus far only been configured with a single k_θ value. Nonetheless, the combination of the target-mirror data, the detailed numerical studies (which include both plasma refraction and a wide spectrum of modes), and the preliminary TEXTOR data, provide solid confirmation of the validity of MIR approach. The TEXTOR experiments will resume in July 2002, and MIR systems will be installed on other tokamaks as access becomes available.

4. SIMULTANEOUS ECEI/MIR

To understand the critical physics issues confronting magnetic fusion; for example, to resolve the relation between anomalous transport and microturbulence, there is a need for simultaneous n_e and T_e fluctuation measurements and successful test results on TEXTOR enable us to design a system to measure both fluctuations simultaneously. Figure 26 illustrates a conceptual design for a combined ECEI and MIR system using refractive optics and dichroic plates to separate the ECEI and MIR signals in frequency space. In order to fulfill this need, a large dichroic plate (~ 20 cm \times ~ 30 cm) was designed and fabricated at the machine shop of NIFS, Japan. The dichroic plate is 1.5 mm thick and contains close-packed holes 1.65 mm in diameter separated by 2.8 mm (center-to-center). This configuration reflects MIR frequencies below 90 GHz while transmitting the ECEI frequencies at 110 GHz or above. In addition, the dichroic plate has been tested for

operation up to 30° from normal incidence and found that the reflected wave fronts and profile are well preserved.

Currently, a combined ECEI and imaging-reflectometer system is under development for the TEXTOR-94 tokamak. In this system, the primary components of a microwave optical system are shared between ECE and reflectometer subsystems, with each subsystem using a dedicated high-resolution multichannel detector array. The basic layout is shown in Fig. 27, including a cross-section of the TEXTOR-94 vacuum vessel, the primary focusing mirrors, and the two diagnostic subsystems.

In an imaging diagnostic, it is essential to make use of as large an acceptance aperture as possible. In the TEXTOR-94 system, the limiting aperture occurs at the vacuum window, which is *42 cm* high, *30 cm* wide, located *57 cm* from the plasma boundary. All other optics have been adapted to make use of the full window aperture.

The primary difference between the configuration of the reflectometry and ECEI subsystems is that the reflectometry system has the added complication of the probing beam. In order to maximize the robustness of the collection optics to details of the plasma profile, the probing beam is focused at the center of the radius of curvature of the cutoff surface, so that the incident wavefront matches the shape of the reflecting layer. The focal point is, of course, different in the poloidal and toroidal directions. The optics are designed so that both the illumination beam and reflected signal can be focused using the two fixed primary mirrors. A beam splitter separates the transmitted beam path from the detection path and final detector optics.

The combined system, including frequency and focal-plane scanning capability, will be completed in 2001 (during an extended TEXTOR-94 maintenance period), to be installed on

5. IMAGING MICROWAVE SCATTERING

Coherent scattering of electromagnetic waves is a powerful technique, capable of providing a direct measure of the spectral power density of fluctuations. It was employed extensively in early studies of plasma turbulence, including the first detection of short scale fluctuations in tokamaks.⁴⁹⁻⁵⁶ In order to measure many wave-numbers simultaneously, a multi-mixer system was employed to study turbulence in tokamaks.^{52,57} With the advent of super-sensitive 2-D detector arrays, it is now feasible to design an imaging microwave scattering system for the investigation of the high k spectra expected from Electron Temperature Gradient (ETG) modes on National Spherical Torus Experiment (NSTX)⁵⁸.

The scattering process is characterized by the differential cross section $\sigma = \sigma_o S(\mathbf{k}, \omega)$, where $\sigma_o = (e^2/mc^2)^2$ is the Thomson cross-section and $S(\mathbf{k}, \omega)$ is the spectral density of density fluctuations. The frequency ω and the wave vector \mathbf{k} must satisfy energy and momentum conservation, i.e., $\omega = \omega_s - \omega_i$ and $\mathbf{k} = \mathbf{k}_s - \mathbf{k}_i$, where the subscripts s and i refer to the scattered and the incident wave, respectively. Since for the case of interest in this paper $\omega_s \approx \omega_i$, and $k_s \approx k_i$, the scattering angle (θ_s) is given by the Bragg equation $k = 2k_s \sin(\theta_s/2)$. Once the spectral density is known, the mean square density fluctuation is obtained by integrating $S(\mathbf{k}, \omega)$ over the entire (\mathbf{k}, ω) space. As discussed in the previous section, \mathbf{k} must satisfy the condition $\mathbf{k} \cdot \mathbf{B} \approx 0$. This and the fact that the direction of the magnetic field lines changes along the propagation of the probing beam can be exploited for the spatial localization of the scattering measurements.

For the measurement of the poloidal spectrum of fluctuations (commonly referred to as the k_θ -spectrum), the probing wave must propagate primarily along a radial direction. In standard scattering experiments, the spatial resolution is determined by the finite size of the probing beam, that here we assume possesses a Gaussian intensity profile $I(r_\perp) = \exp(-2r_\perp^2/w^2)$ (where r_\perp is the beam radius and w the beam waist). The resolution of the measured fluctuation wave number depends on the spectrum $G(\kappa_\perp) = \exp(-\kappa_\perp^2/\Delta^2)$ of the probing beam, where $\Delta = 2/w$ and κ_\perp is the wave number perpendicular to the direction of beam propagation. For $w=5\text{ cm}$, we obtain $\Delta=0.4\text{ cm}^{-1}$, which is indeed very good when compared with the wave numbers (k_\perp) expected in a typical NSTX discharge, as indicated by numerical simulations⁵⁹ showing that the ETG mode occurs in the range of wave numbers $k_\perp\rho_e = 0.1-0.3$ ($10\text{cm}^{-1} < k_\perp < 40\text{cm}^{-1}$). Since the wave vector component along the magnetic field is $k_\parallel \approx 1/qR$ (where q is the magnetic safety factor), the expected fluctuations are nearly constant along the magnetic field lines – a feature that can be used for scattering system design. However, if for the spatial localization we take the common region between the probing and the scattered beam, for $k=10\text{ cm}^{-1}$ we obtain a radial resolution in excess of 60 cm , which is clearly unacceptable. Fortunately, for the case of a probing beam propagating perpendicularly to the magnetic surfaces, the rotation of the magnetic field lines, and therefore the rotation of the fluctuation wave vector \mathbf{k} , can substantially improve the spatial resolution. This was discussed in Ref. [60], where it was shown that the radial resolution is given by an instrumental selectivity function $F(R) = \exp[-(\alpha(R_0) - \alpha(R))^2 (k_\perp/\Delta)^2]$ (where $\alpha(R)$ is the pitch angle of the magnetic field lines and R_0 is the radial location where the matching conditions are tuned for the detection of

fluctuations with wave number k_{\perp}). The radial width of $F(R)$ is a strongly decreasing function of both the magnetic shear (i.e., the derivative of α) and the parameter $(k_{\perp}w)^2$.

Figure 28 illustrates a scattering geometry for the measurement of the k_{θ} -spectrum, where a Gaussian beam with a wavelength of ~ 1 mm and a waist of 2 cm is launched along a trajectory that is nearly tangent to the machine center post (represented by the smallest circle in Fig. 28). Since the beam propagates at a small angle to the density gradient, its trajectory is only slightly affected by plasma refraction. For the case shown in Fig. 28, where the density profile is that of a typical NSTX discharge with a central density of $4.5 \times 10^{19} \text{ m}^{-3}$, the total deflection is $\approx 1^{\circ}$. Plasma theory indicates that the ETG mode, as is the case for many other types of short-scale tokamak instabilities, has a strong ballooning structure. Therefore, the scattered waves will originate mainly on the low field side of the torus. In Fig. 28, they are collected by a spherical mirror and reflected downward where measurements are made on the 2-D receiver array. As a demonstration of the excellent spatial and wave number resolutions that is possible to achieve with this type of scattering configuration, Fig. 29 shows the position of the scattered beam on the focal plane for different wave numbers and scattering locations. In this figure, the beam footprint is represented by a circle having a radius equal to the waist of the beam itself (≈ 0.5 cm), and for each value of k_{\perp} , the scattering location is moved from $R=1.20$ m to 1.46 m in steps of 3.25 cm (from left to right in Fig. 29). The full length of the radial scan is determined by the dimensions of the viewing window, which in Fig. 29 are assumed to be 0.2 m in the x -direction and 0.4 m in the z -direction (even though ports with a maximum size of 0.6 m \times 0.6 m are available in NSTX). A measure of the radial spatial resolution that can be achieved with this type of scattering geometry is obtained from the ratio of the diameter of a circle to the distance of adjunct points

with the same value of k_{\perp} , i.e., the radial resolution is the product of this ratio with the radial separation of the points of origin along the trajectory of the probing beam ($=3.25$ cm).

6. CROSS-POLARIZATION SCATTERING IMAGING

The systems that have been described thus far, ECE imaging and microwave imaging reflectometry, yield information on fluctuations in the electron temperature and density. However, for a complete understanding of anomalous transport in hot magnetized plasmas also the measurement of magnetic field fluctuations is required. Specifically, magnetic field fluctuations as small as $\tilde{B}/B = 10^{-4}$, are sufficient to destroy the often assumed nicely layered field structure thereby resulting in chaotic field distributions. As described below, the magnetic field fluctuations can be measured by means of an imaging system based on cross polarization scattering.

Direct proof of the existence of magnetic field fluctuations with $\tilde{B}/B = 10^{-4}$ in the plasma core is extremely difficult to provide. The only method that has been successfully applied thus far is cross polarization scattering. At the Tore Supra tokamak, this method demonstrated for the first time that such low-level magnetic field fluctuations of with $\tilde{B}/B \cong 10^{-4}$ indeed do exist^{61,62}. More recently, cross polarization scattering was also applied to measure low-frequency electromagnetic waves in the GAMMA-10 tandem mirror⁶³. Electromagnetic waves traveling in the plasma perpendicular to the magnetic field can be scattered by density fluctuations as well as by magnetic field fluctuations. According to scattering^{64,65}, the scattering by density fluctuations will have no effect on the polarization of the wave. However, scattering by magnetic field fluctuations is accompanied by a conversion of the polarization from O- to X-mode or vice versa.

Unfortunately, the cross polarization scattering cross sections are extremely small. Together with the very low level of magnetic field fluctuations one wishes to detect, this implies that one requires an extremely sensitive and delicate detection system. Another problem is also the noisy environment with many chances for spurious mode mixing because of reflections on the inner vacuum vessel wall as well as the mode purity of the injected microwave beam.

It has been pointed out that the scattering cross section can be increased by selecting the frequency of the waves close to the upper-hybrid resonance frequency⁵³⁻⁵⁵. According to linear theory, the cross section for mode conversion is proportional to $(\omega_{wave}^2 - \omega_{UH}^2)^{-2}$. Close to the upper-hybrid frequency, the cross section would go to infinity and clearly linear theory would become invalid. The necessary nonlinear theory is not complete yet, although a good start has been made^{66,67}. By using frequencies close to the upper-hybrid frequency, much larger signals are obtained and, hence, more robust detection systems can be employed. However, the disadvantage of this enhanced cross polarization scattering is that one has great uncertainties in the proportionality factor between signal level and magnetic fluctuation level.

The enhanced cross polarization scattering has been pioneered on the RTP tokamak⁶⁸⁻⁷⁰ and FT-1 tokamaks⁷¹. In the measurements at RTP, the enhanced cross polarization scattering was observed parasitically by a special detection system to monitor the power deposition profile of a 60 GHz, 200 kW Electron Cyclotron Resonance Heating (ECRH) system. Under normal conditions, the detectors are always operated in O-mode polarization to observe the transmitted ECRH power that is launched in O-mode. In order to check the background noise due to wall reflections, some of the detectors were (by serendipity) placed in X-mode. Surprisingly, large signals were received (see Fig. 30), up to several percent of the input power level. The RTP team

investigated many possible explanations for the observed mode conversion. Many of these could be false and the only explanation that still stands is that the high level of X-mode signal is caused by enhanced mode conversion scattering near the upper-hybrid layer in the plasma.

As mentioned above, the system at RTP was originally not built for the purpose of cross polarization scattering measurements. Moreover, because of the fact that nonlinear scattering theories are still in the development phase, it has not been possible to deduce the level of magnetic field fluctuations quantitatively. An advanced system to quantitatively diagnose magnetic field fluctuations has been proposed by Donné and Oomens⁷⁰. Although this system was never built because of lack of funding related to the complexity of the system with many individual detectors and waveguide systems, it will be argued below that imaging techniques would lead to a very simple and versatile cross polarization scattering imaging system allowing to quantitatively determine the level of magnetic field fluctuations.

A cross-correlation scattering experiment as sketched in Fig. 31 is proposed for measuring the local magnetic field fluctuations. Radiation from two sources is injected into the plasma. The waves are launched in X-mode from the high field side of the tokamak. An imaging system at the low field side is employed to detect radiation converted from X- to O-mode. By applying cross-correlation techniques between the different detector elements, it is possible to pin down the mode conversion to the intersection volume of the two microwave beams and thereby improve the spatial resolution beyond what is possible with a small-angle scattering experiment of a single wave.

One reason for using two separate microwave sources is that when only a single source is employed (with two launchers), the outcome of the correlation function would also depend on

the noise of the source. It is necessary to determine which part of the signal received by each detector element is originating from which source, to discriminate the wanted signal from the one source from the scattered signal from the other and vice versa. Using two sources with slightly different carrier frequencies, e.g. several tens of MHz difference, makes it possible to perform such a discrimination without noticeably affecting the position of the upper hybrid layer. By changing the frequencies of both sources simultaneously, it is possible to scan the upper-hybrid layer through the plasma. In this way, measurements can be performed away from the upper-hybrid resonance where linear theory relates the signal level in a straightforward way to the magnetic field fluctuation level. By shifting the upper-hybrid layer into the scattering volume, the same magnetic field fluctuations lead to a much higher signal because of the enhanced mode conversion. In this way, the nonlinear scattering theory can be beautifully tested, at the same time yielding a 'calibration factor' for the enhanced scattering.

It would be optimum if the angle of the launching beams as well as the focusing of the antenna could be changed on a shot-to-shot basis. This would make it possible to place the scattering volume at various locations in the plasma. However, most tokamaks have only limited space at the high field side, such that most probably the launching angle and focusing are rather fixed. Instead of having two individual launchers, it is therefore proposed to have a poloidal array of launchers build in at the high field side, such that it is possible to switch the microwave sources to different launchers between subsequent tokamak shots. Special attention should be devoted to have beams with a small toroidal divergence, because for non-perpendicular injection with respect to the magnetic field also density fluctuations can cause mode conversion scattering, which could mask the desired signal from the magnetic field fluctuations. The effects of magnetic shear as well as polarization mismatch of the mode at the plasma edge have been

Invited Review Article: Review of Scientific Instruments, 2002

considered already in literatures^{62,65} and are not expected to give large problems in the interpretation of the data. Furthermore, care should be taken that the launched signal is pure X-mode, without any spurious O-mode. The Tore Supra team has already demonstrated that this is achievable^{61,62}.

In theory, the reversed set-up (launching O-mode from the low field side and detecting X-mode at the high field side), which was also employed in the RTP pilot experiment, has the additional benefit that the X-mode cutoff layer reflects any spurious O-mode signal in the launching beams, making the launching system more simple. However, the drawback is that the receiver system is located at the high field side, ruling out the use of imaging techniques.

7. PHASE IMAGING INTERFEROMETRY

In addition to the systems described above, imaging techniques have also been applied to both interferometry and polarimetry. However, both space limitations and the fact that these have been extensively covered elsewhere led to the decision to refer the reader to the literature^{10,11,72-76} to all but the most recent developments. Early imaging work involved the use of microbolometer arrays as the detector element⁷⁷⁻⁸¹ and explored tomographic reconstruction techniques. The more recent work on the GAMMA 10 magnetic mirror device utilized Schottky diodes for increased sensitivity and frequency response⁸⁰⁻⁸⁴ and is described in detail in the following.

A millimeter-wave two-dimensional imaging system has been developed for application on the GAMMA 10 tandem mirror device at the University of Tsukuba. It consists of a quasi-optical transmission line with parabolic and ellipsoidal mirrors and a heterodyne receiver with a

frequency of 70 GHz and is comprised of a hybrid detector array with 16 elements of beam-lead GaAs Schottky barrier diodes (SBDs) bonded to bow-tie antennas on a fused-quartz substrate.

The schematic of the 2D imaging system on GAMMA 10 is shown in Fig. 32. It is installed in the west plug cell ($z=971$ cm, outside of a confining potential), where z is the axial distance from the central-cell midplane⁸⁴. The optical system of the probe beam is designed using Gaussian-beam propagation theory. A scalar-feed horn produces a symmetric radiation pattern with low side lobes, which is well fit by a Gaussian distribution. The probe beam is expanded by an off-axis parabolic mirror installed inside the vacuum vessel to cover the upper-half of the plasmas. The cross section of the probe beam is 200 mm \times 200 mm at the plasma center. The receiving optics, consisting of an ellipsoidal mirror, a flat mirror, and polyethylene lenses, are designed by using a ray-tracing method to focus radiation signals onto a 2D-detector array. The magnification of the optical system is designed to be 0.33. The detector array consists of beam-lead GaAs Schottky barrier diodes bonded to 4 x 4 bow-tie antennas and is described later in the technology section. The array is installed inside an aluminum box for electrical shielding, and a 2D pyramidal horn antenna array in TE₁₀ mode is attached to the input of the detector. A dichroic plate, comprised of 10 mm thick aluminum with 4.0 mm diameter holes and 4.5 mm spacing, is also attached to the vacuum window of the receiver side. Circular holes act as high pass filters to prevent the mixture of electron cyclotron resonance heating (ECRH) power with a frequency of 28 GHz.

The imaging system is configured as a heterodyne interferometer consisting of two separate 70 GHz oscillators. An Impatt oscillator with 500 mW output provides a probe beam injected into the plasma and a low-power reference signal. The other 500 mW Impatt oscillator is used as a

local oscillator (LO), which is also divided into two signals. One of the LO output and the probe beam are superimposed coaxially by a beam splitter, and focused on the detector array to produce a 150 MHz IF signal. The branches from the two sources are also combined by a directional coupler and fed to a mixer to provide another IF signal. The quadrature-type detection system provides the phase difference between the two IF signals which is proportional to line density of the plasma. The 2D imaging array has also been applied to ECE measurements using a heterodyne receiver. The second-harmonic ECE signals in the ordinary mode are mixed with LO power on the detector array. The IF signals amplified by 85 dB are fed to the band pass filter with pass band of $100\text{ MHz} \pm 10\text{ MHz}$, and are square-law detected. The ECE imaging in the ordinary mode and the phase imaging can be obtained simultaneously.

The Airy pattern of the point source is measured in order to confirm the performance of the optical system. A Gunn oscillator is located at the position corresponding to the plasma center. The source is imaged onto the detector array. The Airy patterns in the horizontal and vertical planes are shown in Fig. 33. The theoretical curves correspond to the Airy function, which gives an intensity distribution of point image by an ideal lens as

$$I(\rho) = \left[\frac{2J_1(\pi\rho/F_e\lambda)}{\pi\rho/F_e\lambda} \right] \quad (1)$$

where J_1 is the Bessel function of the first kind, ρ the distance from the image point, $F_e=1.17$ the effective F number of the receiving optics, and λ is the wavelength of the source. A good agreement between experiment and theory is obtained in both planes. Magnification of the

optical system is also investigated experimentally by using a point source, which agrees well with the designed value of 0.33.

The system is tested to provide diffraction-limited phase images using a dielectric target located at a position corresponding to the plasma center. Figure 34 shows the 2D image of a Teflon plate of $10.1\text{ mm} \times 10.1\text{ mm}$ size and 1.5 mm thickness in the horizontal and vertical directions. The experimental results are compared with the theoretical curve given by

$$\phi(\rho) = \sqrt{\frac{2}{\pi}} \phi_0 \left\{ S_i \left[2\pi f_0^E (\rho + a) \right] - S_i \left[2\pi f_0^E (\rho - a) \right] \right\} \quad (2)$$

where $2a$ is the width of the object, f_0^E the spatial cutoff frequency, and ϕ_0 and $S_i(x)$ are the sine integral and pulse height functions, respectively⁷⁴. The theoretical curve of the phase distribution is calculated by Fourier-transforming the spatial pulse function into the frequency domain, filtering out all frequency components above f_0^E , and transforming back to the spatial domain. The fitting curve of the experimental points (dotted lines) is drawn by using the Whittaker-Shannon sampling theorem. The good agreement between the experiment and the theory for both phase shift and magnification verifies the validity of this 2D imaging system.

of $10.1\text{ mm} \times 10.1\text{ mm}$ size and 1.5 mm thickness in horizontal and vertical directions.

In each plug/barrier cell of GAMMA 10, two separate 28 GHz gyrotrons are used. Fundamental ECRH in the plug region (ECRH-P) and second-harmonic ECRH in the barrier region (ECRH-B) produce warm and hot electrons that are necessary for effective formation of confining (plug) potentials with thermal barriers. The changes of the density profiles during the

application of the ECRH are shown in Fig. 35. When the ECRH power is applied at $t=140$ ms, the plug potential is created near the position of $z=962$ cm where the magnetic field strength equals to 1 T. At the region of $z=971$ cm where the imaging system is installed, the loss particles decrease due to the formation of the confining potential. When the ECRH is turned off at $t=190$ ms, the confining potential disappears, and a short burst appears in the line-density signal corresponding to the axial drain of the plasmas. The variation of the profile in the axial direction is caused by the change of the magnetic field. It is noted that the density profile in the core region decreases during the injection of the ECRH power. This region corresponds to the one that the effective confining potential is formed. It also coincides to the radial profile of the plug-ECRH power deposition. The phase resolution of the interferometer is estimated to be less than 1/200 fringe, where 1 fringe is equal to a line density of 5.1×10^{13} cm² at 70 GHz.

The imaging array has also applied to the measurement of ECE on GAMMA10. In the present experiment, the optical thickness of the second-harmonic O-mode is estimated to be less than 1 in the plug-cell plasma. Therefore the intensity of the ECE is given by $I_2^{(O)} \propto n_e T_e^3$. Figure 36 shows the time evolution of the ECE profiles where the contour plots display the 2D ECE intensity. Since the frequency of the LO is fixed at 70 GHz, the ECE intensity is distributed around the position $z=969.5$ cm where the frequency of the ECE equals to 70 GHz. The ECE signal starts to increase when the ECRH power is injected at $t=90$ ms and continues to be observed after the bulk plasma disappears at $t=150$ ms. This means that the ECE signal is mainly attributed by the mirror-trapped hot electrons. The hot electrons with energy up to 60 keV are produced by a combination of the plug-ECRH and barrier-ECRH powers, which is useful for the formation of thermal barrier potentials in a tandem mirror plasma.

8. IMAGING ARRAY DEVELOPMENT

Both hybrid and monolithic imaging arrays have been fabricated at UC Davis for use in plasma imaging applications^{85,86}. The hybrid arrays have been comprised of printed circuit slot bowtie antennas coupled with beam lead diodes that are silver epoxied onto the feed of the individual antennas. Shown in Fig. 37 are a mask layout of an ECEI array (a), and a photograph of a hybrid SBT array assembly (b). The monolithic arrays differ in that the diodes are monolithically integrated directly onto the antennas for improved response (necessary for precision in-situ hot-cold load calibrations), reproducibility, and reduced hand labor. The slot bowtie antenna structure has been utilized due to its relatively broad operating bandwidth (~15%), and because of the successes that have been achieved to date with this design. Shown in Fig. 38 are photographs of a monolithic SBT array and the array assembly with the printed circuit board. The antenna patterns of the monolithic array at *100 GHz* are shown in Fig. 39.

More recently, a different class of imaging arrays is under development, which utilize dual dipole antennas [Fig. 40(a)], and which exhibit broad frequency bandwidth similar to the slot bowtie antennas in our present ECEI and MIR systems. The dual dipole antennas, however, offer symmetric E- and H-plane patterns without the large sidelobe levels of the slot bowties [Figs. 40 (b) and (c)]. This should translate to simpler focusing optics and increased sensitivity over the present systems. The first of the new hybrid test antennas has now been fabricated and tested. Monolithic arrays are currently under fabrication and expected by Fall 2001. It is anticipated that the monolithic arrays should exhibit higher sensitivity and reduced LO power requirements over their hybrid counterparts, due to the reduced size and increased cutoff frequency of the monolithic GaAs Schottky diodes.

Invited Review Article: Review of Scientific Instruments, 2002

Another recent development is the replacement of the double sideband detection scheme based on a frequency scanning BWO with a fixed frequency LO source in a single side band detection ECEI system. Here, the IF frequency range extends from 2 to 10 GHz. For each mixer channel, the IF signal is split into 8 signals by band-pass filters separated by 1 GHz, each with a bandwidth of 400 MHz. The sample volumes along the sight lines are separated by about 2 cm, and the sample volume thickness due to the relativistic and Doppler broadening is also about 2 cm. This approach also benefits from the recent advances in millimeter wave technology where single chip MMIC amplifiers have demonstrated 427 mW output at 95 GHz⁸⁷, 2.4 W in a waveguide combined system⁸⁸, and amplifiers have been produced at D-Band (110-170 GHz). Yet another approach to realizing appreciable the required local oscillator power for large ECEI arrays is via frequency multiplication. This is predicted to yield 100 mW at W-band in a MMIC realization⁸⁹ and has yielded 5 W in a quasi-optical frequency tripler grid array⁹⁰ at 99 GHz in a pulsed proof-of-principle experiment with recent activities aimed at a cw realization. Two recent reviews provide an excellent overview of the current state-of-the-art in spatial power combining^{91,92}.

Another approach to solving the LO problem for large arrays is to utilize a subharmonic mixer arrangement where the LO is at half the signal frequency. For example, recently Gauthier *et al.* reported a 140-170 GHz, uniplanar subharmonic mixer with ~13 dB conversion loss⁹³. Such a system is under development for W7-AS⁹⁴ where a 150 GHz MMIC subharmonic mixer array is employed.

In a collaboration between the University of Tsukuba and Tohoku University, 2-D arrays have been developed for both imaging interferometry and ECEI on the GAMMA 10 tandem

Invited Review Article: Review of Scientific Instruments, 2002

mirror device⁹⁵⁻⁹⁹. These are 4×4 arrays of GaAs beam-lead Schottky diodes bonded onto bow-tie antennas monolithically fabricated on 38.1 mm square fused quartz substrates (see Fig. 41). The bow tie angle of 60° results in a resistive antenna impedance of 150Ω .

In a collaboration between Kyushu University and the Teratec Corp.¹⁰⁰, a MMIC detector has been developed for a second harmonic ECEI system ($120\text{-}180 \text{ GHz}$) on LHD consisting of the integration of a bow-tie antenna, a down-converting mixer employing a Schottky barrier diode, and heterojunction bipolar transistor (HBT) amplifiers (10 dB gain) on a GaAs substrate. Figure 42 (a) is the first mask pattern, and (b) is a more recent one. The GaAs chip sizes are $4.0 \text{ mm} \times 2.0 \text{ mm}$ and $2.0 \text{ mm} \times 2.0 \text{ mm}$, respectively and are mounted on the case made of gold-plated brass together with the alumina substrate for dc bias of the SBD and HBT amplifier. In Fig. 42 (b), a coplanar waveguide (CPW) is directly connected to the bow-tie antenna, and the Schottky barrier diode is inserted between the signal and the ground line of the CPW. The lower cutoff frequency increases up to 44 GHz due to the small size of antenna; however, an improvement in IF bandwidth is expected. The heterodyne characteristics of the MMIC detector are measured in a test stand using two oscillators in the frequency range of $70\text{-}140 \text{ GHz}$. One oscillator is employed as an LO and the other supplies a radio frequency (RF) signal. The two signals are combined by a directional coupler, and radiated to the detector through a waveguide antenna. The DC bias of the SBD is typically 0.9 V , 0.5 mA and the power supply of the HBT amplifiers is 4.0 V , 12 mA . The heterodyne IF signal is fed to a spectrum analyzer. Figure 43 shows the heterodyne signal intensity as a function of IF frequency measured with a spectrum analyzer. It is noted that rather flat response from 0.2 GHz to 9 GHz is obtained in contrast to a hybrid detector using a beam-lead SBD, which is probably due to the method of housing of the semiconductor

chip as well as due to the small inductance of the signal line and the performance of SBD. Currently, however, the IF bandwidth is limited to $9\text{-}10\text{ GHz}$. This is primarily caused by the bandwidth of the HBT amplifiers. In Fig. 43, the heterodyne characteristics are also shown with and without HBT amplifiers. The IF bandwidth is limited mostly by the characteristics of the HBT amplifiers in the present stage. An IF bandwidth in excess of 10 GHz is observed without the HBT amplifier. The heterodyne characteristics of the recent MMIC detector are also measured at 140 GHz . The IF response is $\sim 20\%$ better than that of the first design.

Another interesting approach to be considered for the future is direct amplification of the ECE signal, with subsequent filtering and video detection. This is facilitated by the recent developments in InP HEMT based MMICs which have yielded gain up to 184 GHz with noise levels as low as 3.8 dB in D-Band¹⁰¹⁻¹⁰⁷. An example of the direct amplification approach is the passive millimeter wave camera developed by TRW, which operates at 89 GHz with a frame repetition rate of 17 Hz ¹⁰⁸. A camera operating at 140 GHz is also under development¹⁰⁹. Two dimensional tapered slot antennas are utilized in the focal plane of the imaging optics of these cameras. In a plasma diagnostic application, one can employ a microelectromechanical (MEMS) based, active tunable bandpass filter array for frequency discrimination.

9. PHASED ANTENNA ARRAY DEVELOPMENT FOR MIR

As mentioned previously, the need for MIR has been well documented through detailed reflectometry studies by Mazzucato which have revealed the crucial importance of reflectometric imaging (together with the failure of standard fluctuation reflectometry) where the (virtual) reflecting cutoff layer (Fig. 19) is imaged onto the detector plane. This addresses the problem

Invited Review Article: Review of Scientific Instruments, 2002

that ray refraction by the plasma deviates the beam paths; the existence of a “virtual cutoff” layer, located behind actual cutoff, where ray asymptotes arrive at a common focal plane and the field fluctuations are minimum, enables optical imaging of rays.

As discussed in the MIR section, an imaging reflectometry system requires that the wavefront of the probing beam match that of the cutoff surface. For example, a fixed frequency reflectometer system will require a shorter radius of curvature when probing low density plasmas (whose reflecting layer may be located near the plasma core) than when probing high density plasmas (whose layer may move considerably closer to the plasma edge). Also, the various plasma modes have vastly different profiles. This obviously poses a serious constraint on the design of the imaging reflectometer system.

A solution to this instrumental requirement is to develop an electronically controlled “lens” whose focal properties can be adjusted to the particular plasma of interest. A realization of such a “lens” involves the use of phased antenna arrays (PAAs) where a quadratic phase shift is programmed across the array using true time delay generated by nonlinear delay lines (NDLs)¹¹⁰⁻

113.

Figure 44 illustrates the NDL principle whereby the propagation velocity on a varactor diode loaded transmission line is varied by changing the varactor diode bias voltage.

$$v_{prop} = 1 / \sqrt{LC(V)} \quad (9)$$

For frequencies well below the Bragg cutoff, this provides frequency independent true time delay. UC Davis has fabricated both hybrid and monolithic nonlinear delay lines, and shown in Fig. 45 is an example of the latter.

Using an array of linearly tapered slot antennas preceded by NDLs, one has the capability to scan in the desired direction by electronically controlling the bias voltage of each NDL. Moreover, one can also focus/defocus the beam by arranging the bias to generate concave (focusing) or convex (defocusing) wave fronts as shown in Fig. 46. Shown in Fig. 47 is a photograph of a beam control PAA integrated with linearly tapered slot antennas^{61,62} and monolithic NDLs, which has a $\pm 15^\circ$ beam steering range in the 6-18 GHz region.

The block diagram of such an NDL-based beam focusing/defocusing antenna array currently under development for the TEXTOR-94 MIR system is shown in Fig. 48. This focusing/defocusing array system will be operated at 88 GHz with 10% bandwidth. To ensure adequate signal power level at the imaging receivers, the output power of this array should be at least 50 mW to overcome the system loss and scattering loss from the plasma. The desired variable 3-dB beam width extends from 15° to 25° . The envisioned system structure shown in Fig. 49 will be similar to that of the previous NDL-based PAA work. To satisfy the power requirement and to ensure that the NDLs operate at appropriate power levels, a GaAs MMIC chip amplifier providing $15\text{-}17\text{ dB}$ gain will be inserted after each NDL to provide 10 mW output per channel.

An additional approach involves microelectromechanical systems (MEMS) in which the delay lines of the PAA are fabricated via MEMS microfabrication techniques¹¹⁴⁻¹¹⁶. UC Davis

Invited Review Article: Review of Scientific Instruments, 2002

has an active program in MEMS microwave varactors and switches, and has successfully fabricated both. Figure 50 displays a photograph of a MEMS switch which has been successfully operated at 75 GHz ¹¹⁴ MEMS switching arrays with 20×20 of these single switches have been fabricated on $630\mu\text{m}$ thickness quartz substrates with unit cell dimensions of $800\mu\text{m} \times 800\mu\text{m}$. The switching speed of the MEMS varactors is considerably slower ($\sim 1-10\ \mu\text{sec}$) than that of the corresponding GaAs varactors ($\sim 1-10\ \text{nsec}$), yet still sufficiently fast to compensate for the relatively slow ($\gg 1\ \text{msec}$) movements of the plasma cutoff layer. Yet another approach is to employ a quasi-optical array of MEMS switches which would function as an electronically-controlled zone-plate lens which would be placed at the aperture of a microwave horn and thereby obviate the need for the W-band MMIC amplifiers and NDLS. Finally, another interesting approach to beam control has been conceived by K. Chang of Texas A&M who utilizes a piezoelectric translator-driven perturber to vary the propagation velocity along low loss microstrip lines^{117,118}. Beam steering of -34 to $+26$ degrees has been demonstrated at $26.5\ \text{GHz}$ ¹¹⁸ and delay measurements have been made at frequencies as high as W-Band ($75-110\ \text{GHz}$)¹¹⁹. Although slower than either of the above technologies, this still appears to be suitable for the MIR beam shaping application.

10. SUMMARY

Plasma diagnostics has entered an exciting new era where new imaging diagnostics will permit the experimental visualization of turbulence. This is made possible by readily available high performance computing capability and the numerous advances in millimeter wave technology.

11. ACKNOWLEDGMENTS

This work is supported by the U.S. Department of Energy under contract Nos. DE-AC02-76-CH0-3073, DE-FG03-95ER-54295 and W-7405-ENG-48, by NWO and EURATOM, and by the Japanese Ministry of Education, Culture, Sports, Science, and Technology. Assistance from S.R. Burns, R. Hsia, T. Hillyer, and the RTP team is gratefully acknowledged.

12. REFERENCES

1. W. Horton, Drift Waves and Transport, *Rev. Modern Phys.* **71**, pp. 735, (1999).
2. S.E. Parker, W.W. Lee, and R.A. Santoro, Gyrokinetic Simulation of Ion Temperature Gradient Driven Turbulence in 3D Toroidal Geometry, *Phys. Rev. Lett.*, **71**, pp. 2042, (1993).
3. Y. Kishimoto, T. Tajima, W. Horton, M.J. LeBrun, et al., Theory of Self-Organized Critical Transport in Tokamak Plasmas, *Phys. Plasmas* **3**, pp. 1289, (1996).
4. Z. Lin et al., Turbulent Transport Reduction by Zonal Flows: Massively Parallel Simulations, *Science* **281**, pp. 1835-1837, (1998).
5. N. Bretz, "Diagnostic Instrumentation for Microturbulence in Tokamaks", *Rev. Sci. Instrum.* **68**, pp. 2927-2964, (1997).
6. S. Sattler and H.J. Hartfuss, Intensity Interferometry for Measurement of Electron Temperature Fluctuations in Fusion Plasmas, *Plasma Phys. Control. Fusion* **35**, pp. 1285-1306, (1993).
7. E. Mazzucato, "Microwave Imaging Reflectometry for the Visualization of Turbulence in

Invited Review Article: Review of Scientific Instruments, 2002

- Tokamaks”, *Nuclear Fusion* **41**, pp. 203-213, (2001).
8. E. Mazzucato, “Microwave Reflectometry for for Magnetically Confined Plasmas”, *Rev. Sci. Instrum.* **69**, pp. 2201-2217, (1998).
 9. N.J. Lopes Cardozo, F.C. Schuller, C.J. Barth, C.C. Chu *et al.*, *Plasma Filamentation in the Rijnhuizen Tokamak RTP*, *Phys. Rev. Lett.* **73**, 256, (1994).
 10. N.C. Luhmann, Jr., S. Baang, D.L. Brower, S. Burns, A. Chou, E.J. Doyle, J. Howard, Y. Jiang, W.A. Peebles, R. Philipona, C. Rettig, and T.L. Rhodes, “Millimeter and Submillimeter Wave Diagnostic Systems for Contemporary Fusion Experiments: I and II,” *Diagnostics for Contemporary Fusion Experiments, ISPP-9 “Piero Caldirola”*, pp. 135-178, (1991).
 11. N.C. Luhmann, Jr. and W.A. Peebles, “Laser Diagnostics of Magnetically Confined Thermonuclear Plasmas,” in *Laser Handbook*. Academic Press, , Chapter 5, Vol. **5**. Edited by Heinrich Hora and George K. Miley, **6**, pp. 605-619, (1984).
 12. N.C. Luhmann, Jr., *Instrumentation and Techniques for Plasma Diagnostics: An Overview*, in *Infrared and Millimeter Waves*, Academic Press, **2**, Chap. 1, pp. 1-65, (1979).
 13. I.H. Hutchinson, *Principles of Plasma Diagnostics*, New York, Cambridge University Press, (1987).
 14. N.C. Luhmann, Jr. and W.A. Peebles, *Instrumentation for Magnetically Confined Fusion Plasma Diagnostics*, *Rev. Sci. Instrum.* **55**, pp. 279, (1984).
 15. H.J. Hartfuss, T. Geist and M. Hirsch, *Heterodyne Methods in Millimetre Wave Plasma Diagnostics with Applications to ECE, Interferometry and Reflectometry*, *Plasma Phys. Control. Fusion* **39**, pp. 1693, (1997).

Invited Review Article: Review of Scientific Instruments, 2002

16. G. Bekefi, *Radiation Processes in Plasmas*, Wiley: New York, (1966).
17. G. Cima, C. Watts, and R.F. Gandy, Correlation Radiometry of Electron Cyclotron Radiation in TEXT-U, *Rev. Sci. Instrum.* **66**, pp. 798, (1995).
18. G. Cima, et al., “Core Temperature Fluctuations and Related Heat Transport in the Texas Experimental Tokamak-Upgrade”, *Phys. Plasmas*, **2**, No. 3, pp. 720-726, (1995).
19. H.J. Hartfuss and M. Häse, *Temperature Fluctuation Measurements*, Proceedings of the Tenth Joint Workshop on Electron Cyclotron Emission and Electron Cyclotron Heating (EC-10), Ameland, the Netherlands, pp. 119, (1997).
20. C. Watts, et al., “Poloidal Asymmetry and Gradient Drive in Core Electron Density and Temperature Fluctuations on the Texas Experimental Tokamak-Upgrade”, *Phys. Plasmas* **3**, pp. 2013, (1996).
21. C.L. Rettig, et al., “Electron Temperature Fluctuation Measurements and Techniques in the DIII-D Tokamak”. *Rev. Sci. Instrum.* **68**, pp. 484-487, (1997).
22. G. Cima, B. Deng, C.W. Domier, W.R. Geck, R.P. Hsia, C. Liang, F. Jiang, N.C. Luhmann, Jr., and D. Brower, ECE Imaging on TEXT-U, *Fusion Energy and Design*, 34-35, (Seventh International Toki Conference on Plasma Physics and Controlled Nuclear Fusion, Toki, Japan, Nov. 28-Dec. 1, 1996) pp. 515-518, (1997).
23. B.H. Deng, D.L. Brower, G. Cima, C.W. Domier, N.C. Luhmann, and C. Watts, Mode Structure of Turbulent Electron Temperature Fluctuations in the Texas Experimental Tokamak Upgrade, *Phys. Plasmas* **5**, pp. 4117-4120, (1998).
24. B.H.Deng, S.R.Burns, C.W.Domier, T.R.Hillyer, R.P.Hsia, N.C.Luhmann Jr., D.L.Brower,

Invited Review Article: Review of Scientific Instruments, 2002

- G.Cima, A.J.H. Donné, T.Oyevaar, RTP team, ECE Imaging of plasma T_e profiles and fluctuations. *Fusion Engineering and Design* **53**, pp.77-85, (2001).
25. B.H. Deng, et al., “Electron Cyclotron Emission Imaging Diagnostic of T_e Profiles and Fluctuations”, *Phys. Plasmas* **8**, no. 5, pp. 2163-2169, (2001).
26. B.H. Deng, C.W. Domier, N.C. Luhmann, Jr., D.L. Brower, G. Cima, A.J.H. Donné, T. Oyevaar, M.J. van de Pol, “ECE imaging of electron temperature and electron temperature fluctuations (invited)”, *Rev. Sci. Instrum.* **72**, pp. 301, (2001).
27. R.V. Bravenec, A.J. Wootton, *Effects of Limited Spatial Resolution on Fluctuation Measurements*, *Rev. Sci. Instrum.*, **66**, pp. 802, (1995).
28. R.P. Hsia, B. H. Deng, W.R. Geck, C. Liang, C.W. Domier, and N.C. Luhmann, Jr., Hybrid Electron Cyclotron Emission Imaging Array System for Texas Experimental Tokamak Upgrade, *Rev. Sci. Instrum.* **68**, pp. 488, (1997).
29. B.H. Deng, R.P. Hsia, C.W. Domier, S.R. Burns, T.R. Hillyer, N.C. Luhmann, Jr., T. Oyevaar, A.J.H. Donné, and the RTP Team, “Electron Cyclotron Emission Imaging Diagnostic System for RTP”, *Rev. Sci. Instrum.* **70**, pp. 998, (1999).
30. B.H. Deng, C.W. Domier, N.C. Luhmann, Jr., A.J.H. Donné, and M.J. van de Pol, ECE Imaging on TEXTOR-94, *Rev. Sci. Instrum.* **72**, pp. 368-370, (2001).
31. A. Mase, H. Negishi, N. Oyama, K. Watabe, K. Mizuno, Y. Nagayama, K.Kawahata, H. Matsuura, K. Uchida, A. Miura, T. Tamano, and K. Yatsu, “ECE-Imaging Work on GAMMA 10 and LHD”, *Fusion Eng. Design* **53**, pp. 87-95, (2001).
32. A. Mase, M. Ohashi, A. Yamamoto, H. Negishi, N. Oyama, Y. Nagayama, K.Kawahata, K.

Invited Review Article: Review of Scientific Instruments, 2002

- Watabe, K. Mizuno, H. Matsuura, K. Uchida, and A. Miura, "Application of Millimeter-Wave Imaging System to LHD", *Rev. Sci. Instrum.* **72**, No. 1, pp. 375-378, (2001).
33. B.H. Deng, Two Dimensional Electron Cyclotron Emission Imaging Study of Electron Temperature Profiles and Fluctuations of Tokamak Plasmas, PhD dissertation, University of California at Davis, (1999).
34. W. Horton, *et al.*, "Coherent Drift-wave Structures in Toroidal Plasmas", *J. Plasma Phys.* **56**, part 3, pp. 605-613, (1996).
35. B.H. Deng, *et al.*, "Imaging of Core Electron Temperature Fluctuations of Tokamak Plasmas", submitted for publication in the 3rd Triennial Special Issue of the IEEE Transactions on Plasma Science, Images in Plasma Science.
36. E. Mazzucato, "Microwave Reflectometry for Magnetically Confined Plasmas," *Rev. Sci. Instrum.* **69**, pp. 2201-2217, (1998).
37. E. Mazzucato, "Density Fluctuations in the Adiabatic Toroidal Compressor," *Bulletin of The American Physical Society* **20**, pp. 1241, (1975).
38. E. Mazzucato, "Density Fluctuations in the Adiabatic Toroidal Compressor," Princeton University Plasma Physics Laboratory Report MATT-1151, (1975).
39. J.L Doane, E. Mazzucato and G.L. Schmidt, "Plasma Density Measurements Using FM-CW Millimeter Wave Radar Techniques," *Rev. Sci. Instrum.* **52**, pp. 12-15, (1981).
40. E. Mazzucato and R. Nazikian, "Microwave Reflectometry for the Study of Density Fluctuations in Tokamak Plasmas," *Plasma Phys. Control. Fusion* **33**, pp. 261-274, (1991).
41. A. Costley, "Microwave Refeectometry", *Diagnostics for Contemporary Fusion*

Invited Review Article: Review of Scientific Instruments, 2002

Experiments, ISPP-9 “Piero Caldirola”, pp. 113-134, (1991).

42. E. Mazzucato et al., “Turbulent Fluctuations in TFTR Configurations with Reversed Magnetic Shear,” *Phys. Rev. Lett.* **77**, pp. 3145-3148, (1996).
43. E. Mazzucato and R. Nazikian, “Radial Scale Length of Turbulent Fluctuations in the Main Core of TFTR Plasmas,” *Phys. Rev. Lett.* **71**, 1840, (1993).
44. B.I. Cohen, B.B. Afeyan, A.E. Chou, and N.C. Luhmann, Jr., “Computational Study of Ultra-Short Pulse Reflectometry,” *Plasma Phys. Control. Fusion* **37**, pp. 329-344, (1995).
45. C.W. Domier, N.C. Luhmann, Jr., A.E. Chou, W-M. Zhang, and A.J. Romanowsky, “Ultrashort-Pulse Reflectometry (Invited),” *Rev. Sci. Instrum.* **66**, pp. 399-401, (1995).
46. R. Nazikian, G.J. Kramer, and E. Valeo, “A Tutorial on the Basic Principles of Microwave Reflectometry Applied to Fluctuation Measurements in Fusion Plasmas”, *Phys. of Plasmas* **8**, pp.1840-1855, (2001).
47. E. Mazzucato, “Numerical Study of Microwave Reflectometry in Plasmas with 2D Turbulent Fluctuations,” *Rev. Sci. Instrum.* **69**, pp. 1691-1698 (1998).
48. Y. Lin, R. Nazikian, J.H. Irby and E.S. Marmor, Plasma Curvature Effects on Microwave Reflectometry Fluctuation Measurements, *Plasma Phys. Control. Fusion* **43**, L1, (2001).
49. E. Mazzucato, “Small Scale Density Fluctuations in the Adiabatic Toroidal Compressor,” *Phys. Rev. Lett.* **36**, pp. 792, (1976).
50. C.M. Surko and R.E. Slusher, “Study of the Density Fluctuations in the Adiabatic Toroidal Compressor Scattering Tokamak Using CO₂ Laser,” *Phys. Rev. Lett.* **37**, pp. 1747, (1976).

Invited Review Article: Review of Scientific Instruments, 2002

51. E. Mazzucato, "Spectrum of Small Scale Density Fluctuations in Tokamaks," Phys. Rev. Lett. **48**, pp. 1828, (1982).
52. D.L. Brower, W.A. Peebles, N.C. Luhmann, Jr., R.L. Savage, Jr., "Multichannel Scattering Studies of the Spectra and Spatial Distribution of Tokamak Microturbulence," Phys. Rev. Lett. **54**, pp. 689, (1985).
53. D.L. Brower *et al.*, Nucl. Fusion **27**, pp. 2055, (1987).
54. E.J. Doyle, R.J. Groebner, K.H. Burrell, P. Gohil, T. Leheka, N.C. Luhmann, Jr., H. Matsumoto, T.H. Osborne, W.A. Peebles, R. Philipona, "Modification in Turbulence and edge Electric Field at the L-H transition in the DIII-D Tokamaks," Phys. Fluids **B3**, pp. 2300, (1991).
55. H. K. Park, N.C. Luhmann, Jr., W.A. Peebles, and R. Kirkwood, "Observation of Second-Harmonic Ion Bernstein Waves Excited by Fast-Wave Mode Conversion in the Microtor Tokamak," Phys. Rev. Lett. **52**, pp. 1609, (1984).
56. H.K. Park, C.X. Yu, W.A. Peebles, N.C. Luhmann, Jr., and R. Savage, "Multi Mixer FIR Laser Thomson Scattering Apparatus," Rev. Sci. Instrum. **53**, pp. 1535, (1982).
57. H.K. Park, D.L. Brower, W.A. Peebles, N. C. Luhmann, Jr., R L. Savage, and C.X. Yu, "Development and Application of Multichannel Collective Scattering Systems," Rev. Sci. Instrum. **56**, (1985).
58. E. Mazzucato, T. Munsat, H. Park, B.H. Deng, C.W. Domier, and N.C. Luhmann, Jr, A.J.H. Donne and M.J van de Pol, "Fluctuations measurements in tokamaks with microwave imaging reflectometry", Phys. Plasmas, **9**, pp. 1, (2002).
59. W. Dorland, F. Jenko, M. Kotschenreuther, and B. Rogers, Phys. Rev. Lett. **85**, pp. 5579, (2000).

Invited Review Article: Review of Scientific Instruments, 2002

60. P. Devynck, X. Garbet, C. Laviron, J. Payan, S.K. Saha, F. Gerraris, P.H. Hennequin, A. Quemeuneur, A. Truc, "Localized Measurements of Turbulence in the TORE SUPRA Tokamak," *Plasma Phys. Control. Fusion* **35**, pp. 63, (1993).
61. X.L. Zou *et al.*, *Phys. Rev. Lett.* **75**, pp. 1090, (1995).
62. L. Colas, X.L. Zou, M. Paume, J.M. Chareau, L. Guiziou, G.T. Hoang, Y. Michelot, D. Gresillon, *Nucl. Fusion* **38**, pp. 903, (1998).
63. Y. Kogi, A. Mase, L.G. Bruskin, N. Oyama, T. Tokuzawa, S. Kubota, A. Itakura, M. Ichimura, H. Hojo, T. Tamano and K. Yatsu, *Rev. Sci. Instrum.* **70**, pp. 991, (1999).
64. T. Lehner, J.M. Rax and X.L. Zou, *Europhys. Lett.* **8**, pp. 759, (1989).
65. L. Vahala, G. Vahala and N. Bretz, *Phys. Fluids* **B4**, pp. 619, (1992).
66. E.Z. Gusakov and A.D. Piliya, *Sov. Phys. Tech. Phys. Lett.* **18**, pp. 325, (1992).
67. K.M. Novik and A.D. Piliya, *Plasma Phys. Contr. Fusion* **35**, pp. 357, (1993).
68. A.Yu. Stepanov, L. Colas, A.J.H. Donné, E.Z. Gusakov, A.A.M. Oomens, F.C. Schüller and the RTP Team, *Proc. Combined 1998 ICPP and 25th EPS Conf. on Contr. Fusion and Plasma Physics, Prague (1998)*, *Eur. Conf. Abs.* **22C**, pp. 754, (1998).
69. A.A.M. Oomens, W.A. Bongers, F.C. Schüller, F.M.A. Smits and RTP-Team, *Proc. EPS Top. Conf. on Radiofrequency Heating and Current Drive of Fusion Devices, Brussels* pp. 317, (1992).
70. A.J.H. Donné and A.A.M. Oomens, "Enhanced Mode Conversion of Microwaves near the Upper Hybrid Layer as a Diagnostic Tool to Measure Magnetic Fluctuations", *Proc. of the 9th Joint Workshop on Electron Cyclotron Emission and Electron Cyclotron Heating, Borrego*

Invited Review Article: Review of Scientific Instruments, 2002

Springs pp. 645-650, (1995).

71. D.G. Bulyginskiy, A.D. Gurchenko, E.Z. Gusakov, V.V. Korkon, M.M. Larionov, K.M. Novik, A.A.M. Oomens, Yu.V. Petrov, V.L. Selenin and A.Yu. Stepanov, Proc. Combined 1998 ICPP and 25th EPS Conf. on Contr. Fusion and Plasma Physics, Prague (1998), Eur. Conf. Abs. **22C**, pp. 1546, (1998).
72. K.S. Yngvesson, T.L. Korzeniowski, Y-S Kim, E.L. Kollerg, and J.F. Johnsson, “ The Tapered Slot Antenna – A New Integrated Element for Millimeter-Wave Applications,” *IEEE Trans. Microwave Theory Tech.*, **37**, No.2, pp.365-374, (1989).
73. S. Sugawara, Y. Maita, K. Adachi, K. Mori, K. Mizuno, (Edited by R. Meixner), “Characteristics of a MM-Wave Tapered Slot Antenna with Corrugated Edges”. 1998 IEEE MTT-S International Microwave Symposium Digest, pp.533-536, (1998).
74. P.E. Young et al., *Application of Far-Infrared, Integrated Detector Arrays to Chord-Averaged Plasma Measurements*, Rev. Sc. Instrum. **56**, pp. 896, (1985).
75. P.E. Young, N.C. Luhmann, Jr., R.J. Taylor, D.P. Neikirk, and D.B. Rutledge, “Far-Infrared Imaging of Tokamak Plasma,” Rev. Sci. Instrum. **56**, pp. 903-904, (1985).
76. E. J. Doyle et al., *Determination of the Two-Dimensional Density Distribution in a Tokamak Plasma Using Phase-Imaging Interferometry*, Rev. Sci. Instrum. **57**, pp. 1945, (1986).
77. J. Howard et al., *Density Profile Reconstructions from 2-D Interferometric Data on Microtor Using Novel Tomographic Analysis Techniques*, Rev. Sci. Instrum. **59**, pp. 2135, (1988).
78. Neikirk, D.P.; Rutledge, D.B.; Muha, M.S.; Park, H.; Chang-Xuan Yu, “Far-infrared Imaging Antenna Arrays.” *Applied Physics Letters* **40**, pp. 203-205, (1982).

79. Tong, P.P.; Neikirk, D.P.; Young, P.E.; Peebles, W.A.; Luhmann, N.C., Jr.; Rutledge, D.B. “Imaging Polarimeter Arrays for Near-Millimeter Waves.” *IEEE Transactions on Microwave Theory and Techniques*, **MTT-32**, (No.5), pp. 507-512, (1984).
80. K. Hattori, A. Mase, K. Mizuno, A. Itakura, M. Inutake, and S. Miyoshi, Application of Millimeter-Wave Phase-Imaging Interferometry to the Tandem Mirror GAMMA 10, *Jpn. J. Appl. Phys.* **27**, No. 7, pp. 1361-1362, (1988).
81. K. Hattori, A. Mase, A. Itakura, M. Inutake, S. Miyoshi, K. Uehara, T. Yonekura, H. Nishimura, K. Miyashita, and K. Mizuno, Millimeter-Wave Phase-Imaging Interferometer for the GAMMA 10 Tandem Mirror, *Rev. Sci. Instrum.* **62**, No. 12, pp. 2857-2861, (1991).
82. N. Oyama, A. Mase, T. Tokuzawa, Y. Ito, A. Itakura, K. Mizuno, and Y. Harada, Millimeter-Wave Phase Imaging Interferometry using Two-Dimensional Detector Array, *Jpn. J. Appl. Phys.* **34**, No. 4A, pp. 2006-2007, (1995).
83. A. Mase, N. Oyama, T. Tokuzawa, K. Imamura, A. Itakura, T. Tamano, Y. Harada, and K. Mizuno, Application of Millimeter-Wave Two-Dimensional Imaging Array to the GAMMA 10 Tandem Mirror, *Proc. 7th Int. Symp. on Laser-Aided Plasma Diagnostics*, Fukuoka, pp. 240-245, (1995).
84. K. Yatsu, L. G. Bruskin, T. Cho, M. Hamada, M. Hirata, H. Hojo, M. Ichimura, K. Ishii, A. Itakura, I. Katanuma, Y. Kiwamoto, J. Kohagura, S. Kubota, A. Mase, Y. Nakashima, T. Saito, Y. Sakamoto, T. Tamano, Y. Tatematsu, T. Tokuzawa, M. Yoshikawa, *Nucl. Fusion* **39**, pp. 1707, (1999).
85. R.P. Hsia, W.R. Geck, S. Cheng, W-M. Zhang, C.W. Domier, and N.C. Luhmann, Jr., “ECE Imaging Array Diagnostic Development of TEXT-U,” *Rev. Sci. Instrum.* **66**, pp. 834-836,

Invited Review Article: Review of Scientific Instruments, 2002

(1995).

86. Shelley Xiao-Lei Cheng, "Monolithic Schottky-Diode Imaging Array", Master thesis, UCLA, (1993).
87. Y.C. Chen et al. "A 95 GHz InP HEMT MMIC Amplifier with 427 mW Power Output", IEEE Microwave Guided Letters **8**, pp. 399-401, (1998).
88. D.L. Ingram et al., "Compact W-band Solid-state MMIC High Power Sources", in 2000 IEEE MTT-S Int. Microwave Symp. Digest, Boston, MA, pp. 955-958, (2000).
89. E. O'Ciardha, B. Lyons ,and S. Lidholm, "100 GHz MMIC Power Source Development Study", Int. Journal of Infrared and Millimeter Waves, **21**, pp.1747-1759, (2001).
90. Hong-Xia L. Liu, L.B. Sjogren, C.W. Domier, N.C. Luhmann, Jr., D.L. Sivco and A.Y. Cho, "Monolithic Quasi-Optical Frequency Tripler Array with 5 Watt Output Power at 99 GHz", IEEE Electronic Device Letters **14**, pp. 329-331, (1993).
91. J. Harvey, E.R.Brown, D.B. Rutledge, and R.A. York, "Spatial Power Combining for High-Power Transmitters", IEEE Microwave Magazine **1**, pp. 48-59, (2000).
92. M.P. DeLisio and R.A. York, "Quasi-Optical and Spatial Power Combining", to appear in IEEE Trans. on MTT, Special 50th Anniversary Issue, (2001).
93. G.P. Gauthier, J.P. Raskin, and G.M. Rebeiz, "A 140-170 GHz Low-Noise Uniplanar Subharmonic Schottky Receiver", IEEE Trans. on MTT, **48**, pp.1416-1419, (2000).
94. S. Baumel, M. Rodriguez and H.J. Hartfuss, ECE Imaging Development at W7-AS, 26th EPS Conf. on Contr. Fusion and Plasma Physics, Maastricht, 14-18 June 1999. ECA **23J**, pp. 1581-1584, (1999).

Invited Review Article: Review of Scientific Instruments, 2002

95. N. Oyama, A. Mase, T. Tokuzawa, K. Imamura, A. Itakura, T. Tamano, Y. Harada, and K. Mizuno, Millimeter-Wave Two-Dimensional Imaging Array for the GAMMA 10 Tandem Mirror, *Rev. Sci. Instrum.* **68**, No. 1, pp. 500-503, (1997).
96. N. Oyama, A. Mase, T. Tokuzawa, K. Imamura, A. Itakura, Y. Ito, T. Tamano, Y. Harada, and K. Mizuno, Plasma Diagnostics Using Millimeter-Wave Two-Dimensional Imaging Array, *Fusion Eng. Design*, **34-35**, pp. 407-410, (1997).
97. N. Oyama, A. Mase, T. Tokuzawa, A. Itakura, T. Tamano, K. Yatsu, Y. Nagayama, K. Kawahata, K. Watabe, K. Mizuno, A. Miura, H. Matsuura, and Y. Harada, Development of Millimeter-Wave Two-Dimensional Imaging Array for Large Fusion Devices, *Proc. 8th Int. Symp. on Laser-Aided Plasma Diagnostics*, Doorwerth, pp. 343-348, (1997).
98. N. Oyama, A. Mase, H. Negishi, T. Tokuzawa, A. Itakura, T. Tamano, K. Yatsu, K. Watabe, K. Mizuno, Y. Nagayama, K. Kawahata, H. Matsuura, and A. Miura, Development of Millimeter-Wave Two-Dimensional Imaging Array, *Rev. Sci. Instrum.* **70**, No. 1, pp. 1003-1006, (1999).
99. H. Negishi, A. Mase, N. Oyama, H. Matsuura, K. Uchida, A. Miura, Y. Nagayama, K. Kawahata, A Fully Monolithic Millimeter-Wave Detector for Plasma Diagnostics, *Conf. Digest 24th Int. Conf. on Infrared and Millimeter-Waves*, Monterey, TU-D2, (1999).
100. H. Matsuura, K. Tezuka, I. Aoki, M. Yamanaka, S. Kobayashi, T. Fujita, A. Miura, and Y. Nagayama, *Electronics Lett.* **33**, (1997).
101. C. Pobanz, et al., "A High-Gain Low Power MMIC LNA for Ka-Band Using InP HEMTs", *IEEE Radio Frequency Integrated Circuits Symposium*, Edited by M. J. Piscataway, pp. 149-152, (1999).

Invited Review Article: Review of Scientific Instruments, 2002

102. M. Nishimoto et al., "High Performance D-Band (118 GHz) Monolithic Low Noise Amplifier", Proc. of 1999 IEEE Radio Frequency Integrated Circuits Symposium, pp. 99-102, (1999).
103. R. Lai et al., "D-Band MMIC LNAs with 12 dB Gain at 155 GHz Fabricated on a High Yield InP HEMT MMIC Production Process", Proc. 1997 International Conference on Indium Phosphide and Related Materials, pp. 241-244, (1997).
104. D.L. Edgar, et al., "94 and 150 GHz Coplanar Waveguide MMIC Amplifiers Realized Using InP Technology", IEEE MTT-S International Microwave Symposium Digest, **1**, pp. 247-250, (1999).
105. C. Pobanz et al., "A High-Gain Monolithic D-Band InP HEMT Amplifier", IEEE Journal of Solid-State Circuits **34**, pp.1219-1224, (1999).
106. D.C.W. Lo, et al., "MMIC-Based W-Band Dicke Switched Direct-Detection Receiver", IEEE Gallium Arsenide Integrated Circuit Symposium, 17th Annual Technical Digest, San Diego, CA, USA, pp. 226-229, (1995).
107. R. Kuroda, et al., "Direct-Detection MMIC FPAs for MMW Imaging", Proc. SPIE **3064**, pp. 90-97, (1997).
108. P. Moffa, L. Yujiri, K. Jordan, R. Chu, *et al.*, "Passive Millimeter Wave Camera Flight Tests." Proc. of the SPIE - The International Society for Optical Engineering, **4032**, pp.14, (2000).
109. L. Yujiri, S. Fornaca, B. Hauss, *et al.*, "140 GHz Passive Millimeter Wave Video Camera", Proc. of the SPIE - The International Society for Optical Engineering, **3703**, pp. 20, (1999).
110. W. M. Zhang, R. P. Hsia, C. Liang, G. Song, C. W. Domier, N. C. Luhmann, Jr., "Novel

Invited Review Article: Review of Scientific Instruments, 2002

Low-Loss Delay Line for Broadband Phased Antenna Array Applications”, IEEE Microwave Guided Wave Letters **6**(11), pp. 182-184, (1996).

111. R. P. Hsia, W. M. Zhang, C. W. Domier, N. C. Luhmann, Jr., "A Hybrid Nonlinear Delay Line-based Broad-band Phased Antenna Array System”, IEEE Microwave Guided Wave Letters **8**, pp. 182-184, (1998).

112. C. Liang, R. P. Hsia, C.C. Chang, C. W. Domier, N.C. Luhmann, Jr., W. Berk, E. Schlecht, “Wide Band True Time Delay Line Controlled Phased Antenna Arrays ” 24th International Conference on Infrared and Millimeter Waves, U.S.A., p.PM-B5, (1999).

113. C.C. Chang, R.P. Hsia, C. Liang, C.W. Domier, N.C. Luhmann, Jr., “2-Dimensional Nonlinear Delay Line-Based Phased Antenna Arrays” 2nd International Conference on Microwave and Millimeter Wave Technology proceedings, Beijing, China, pp.274-277, (2000).

114. W-K. Zhang, Fan Jiang, C.W. Domier, and N. C. Luhmann, Jr.,” Quasi-Optical E-Band MEMS Switching Arrays”, to be published in Proc. of IEEE International Microwave Symposium, June, (2002).

115. Rizk, J.; Guan-Leng Tan; Muldavin, J.B.; Rebeiz, G.M, “High-isolation W-band MEMS Switches,” IEEE Microwave and Wireless Components Letters, **11**, No.1, IEEE, pp.10-12., (2001).

116. E.R. Brown. “RF-MEMS switches for reconfigurable integrated circuits.” IEEE Transactions on Microwave Theory and Techniques, vol.46, (No.11, pt.2), IEEE, p.1868-1880, (1998).

Invited Review Article: Review of Scientific Instruments, 2002

117. T.-Y. Yun and K. Chang, “ A low loss time-delay phase shifter controlled by piezoelectric transducer to perturb microstrip line”, IEEE Microwave and Guided Wave Letters , **10**, pp. 96-98, (2000).
118. T.-Y. Yun and K. Chang, “A low-cost 8 to 26.5 GHz phased array antenna using a piezoelectric transducer controlled phase shifter”, IEEE Trans. Antennas and Prop., (2001)
119. K. Chang , private communication, (2001)

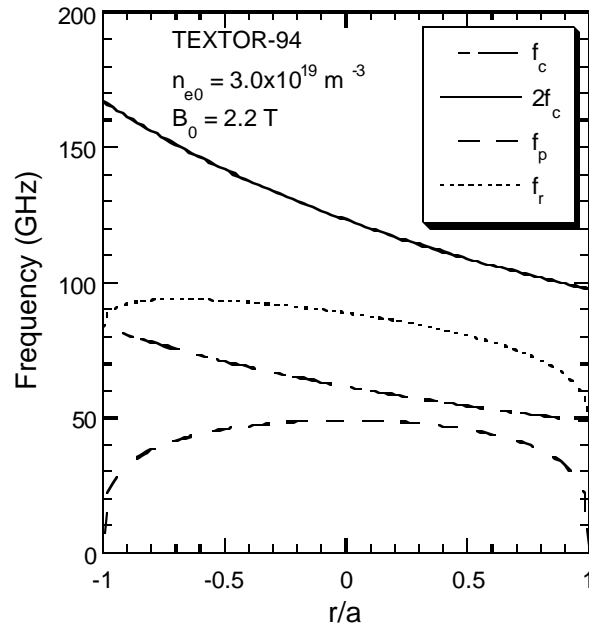


Figure 1. Characteristic frequencies of TEXTOR-94.

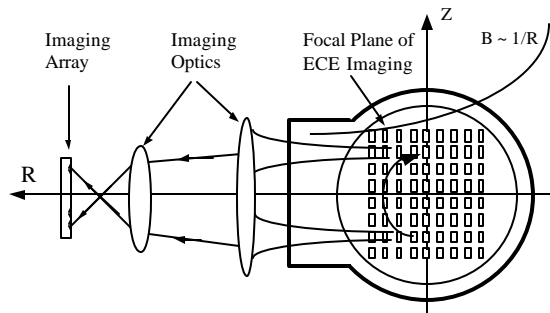


Figure 2. Schematic diagram illustrating the ECEI system principle.

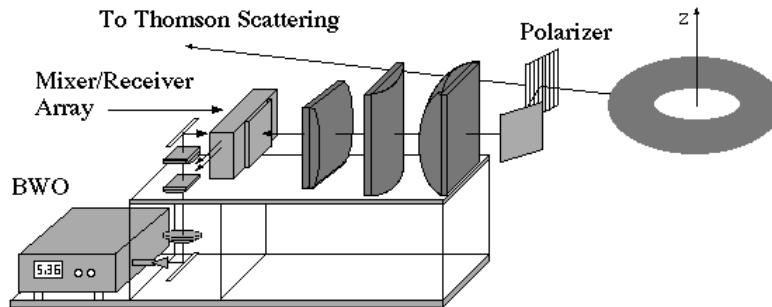


Figure 3. ECEI implementation on the RTP tokamak.

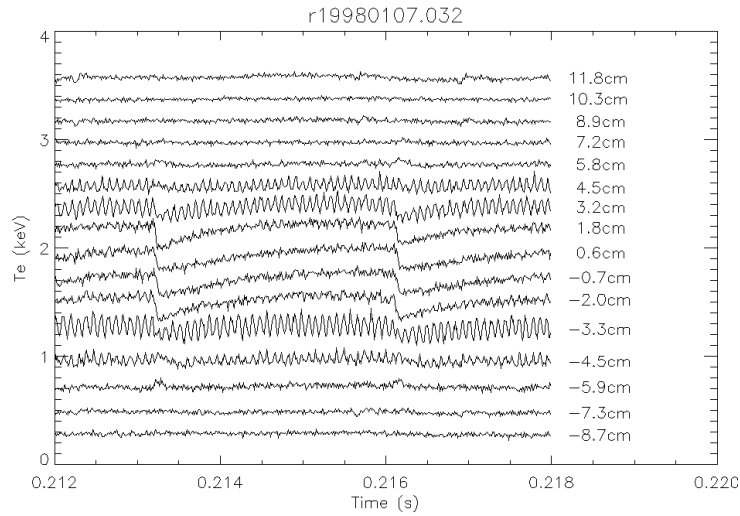


Figure 4. An $m=2$ mode is observed to be localized at the sawtooth inversion radius ($r \sim 3.5$ cm), with a radial extent of less than 2 cm. This mode is very stable, and can survive the sawtooth crashes.

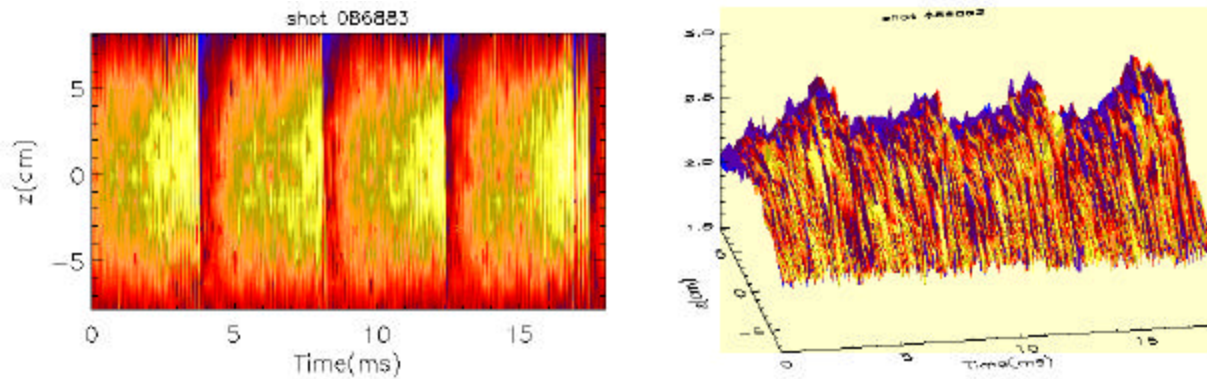


Figure 5. Observation of temperature profiles on TEXTOR-94 with ECEI.

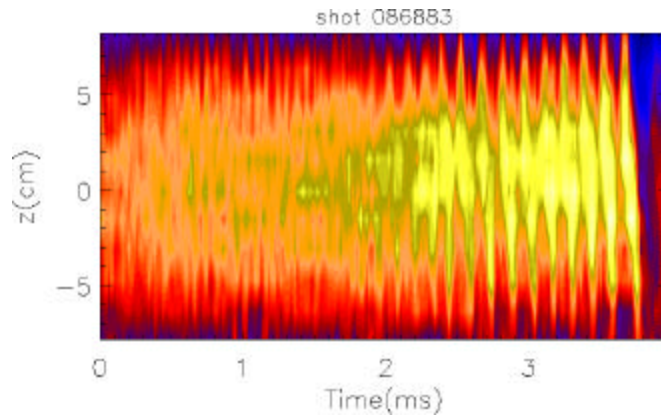


Figure 6. Strong MHD mode in TEXTOR-94 generated by ECRH. Time starts from 1.566 sec. Sensitivity calibrated with Thomson scattering

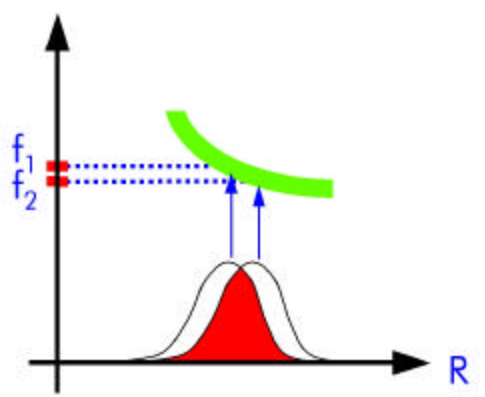


Figure 7. Correlation measurement of local electron temperature fluctuations.

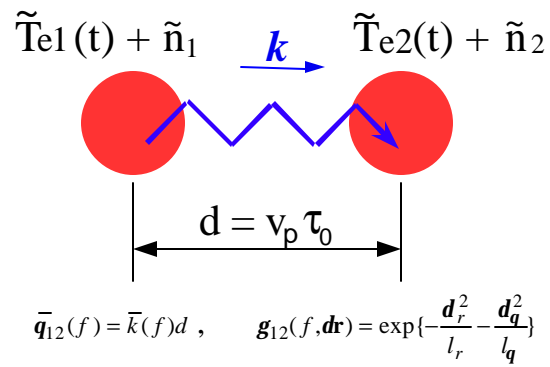


Figure 8. Two point correlation measurement of electron temperature fluctuations.

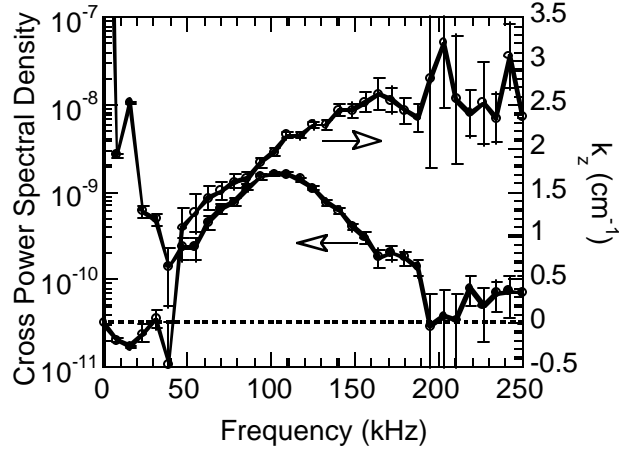


Figure 9. Cross power spectral density and statistical dispersion relation of T_e fluctuations measured at $r/a = 0.7$ during the flat top (0.1 - 0.35 s) of six reproducible discharges, with $I_p = 100$ kA, $\bar{n}_e = 3.3 \times 10^{19} \text{ m}^{-3}$, $B_\phi = 1.88$ T, and $f_{LO} = 120$ GHz. The error bars denote the standard deviation over multiple realizations. The average of the cross correlation function has been subtracted.

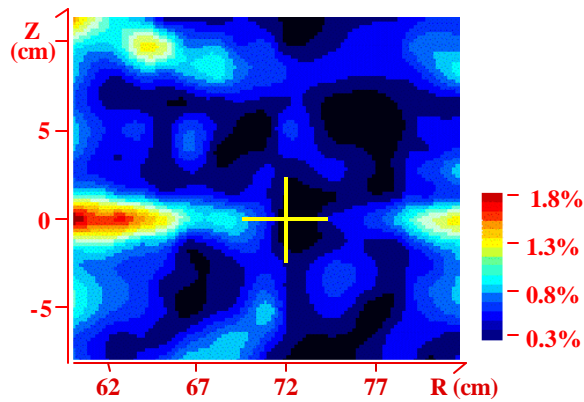


Figure 10. 2-D image of the relative fluctuation level (\bar{T}_{irms}/T_e) of the turbulent fluctuations (30-170 kHz) measured at $I_p = 60$ kA, and $\bar{n}_e = 1.5 \times 10^{19} \text{ m}^{-3}$. The color scale ranges from 1.8% (Red) to 0.3% (dark). The statistical noise level is about 0.3%. R is the plasma horizontal position (72 cm corresponds to the plasma axis) z is the plasma vertical position, and the yellow-cross indicates the center of the vacuum chamber. The data are from about fifty identical discharges.

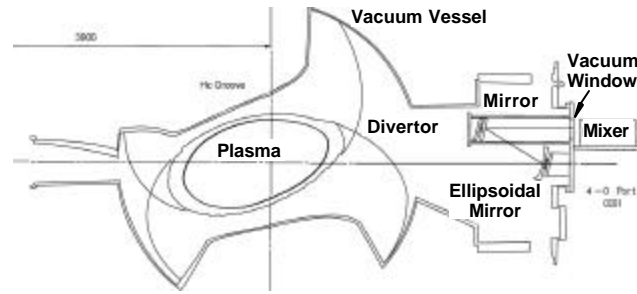


Figure 11. Schematic of the LHD ECEI System.

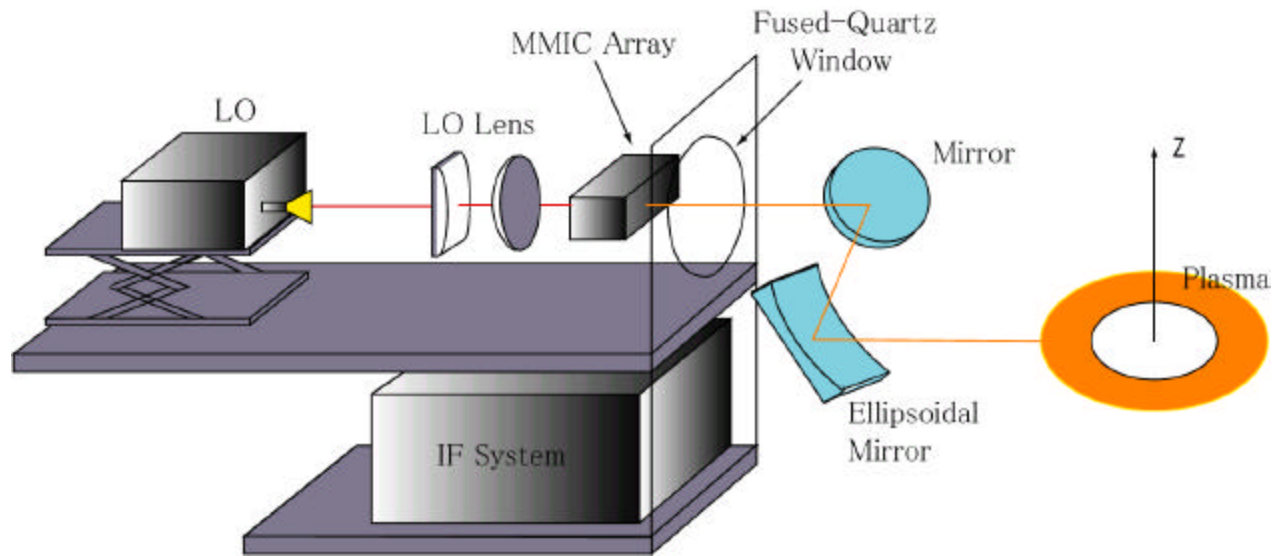


Figure 12. LHD ECEI Experimental Apparatus.

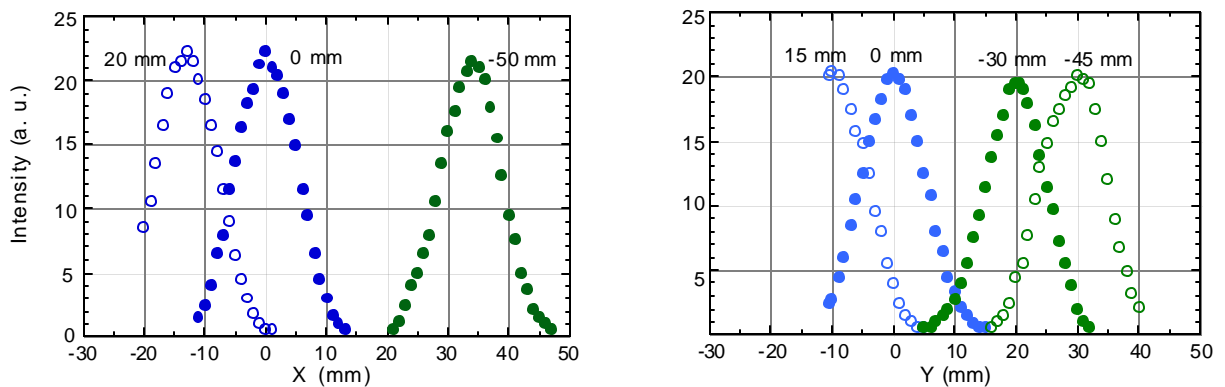


Figure 13. LHD ECEI System Airy Patterns.

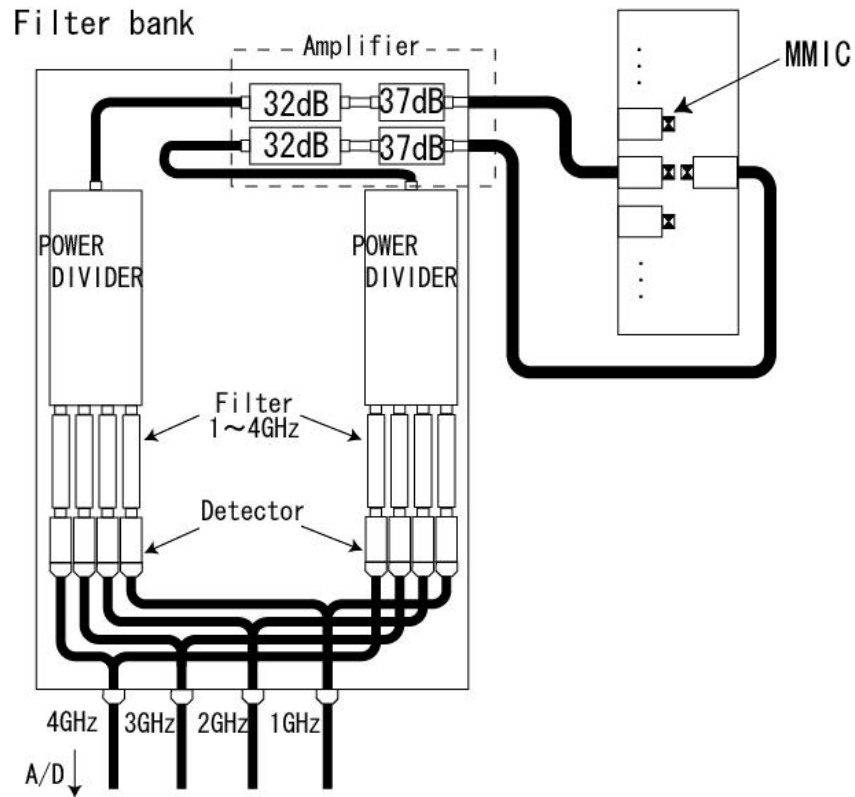


Figure 14. LHD ECEI IF System.

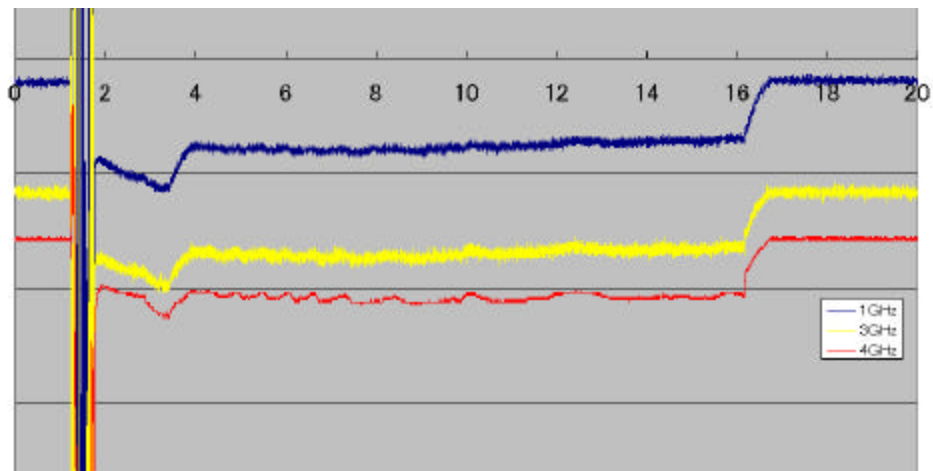


Figure 15. Time evolution of LHD ECEI IF signals.

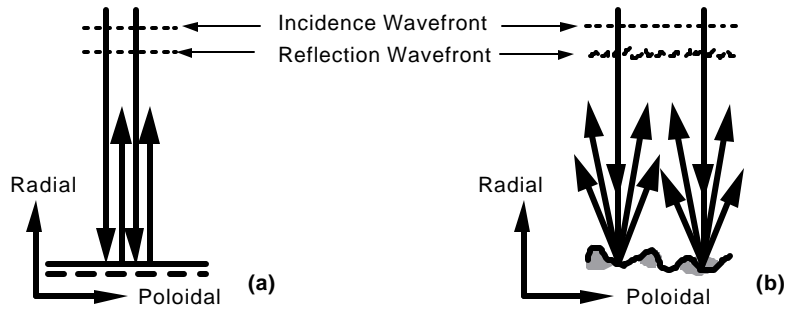


Figure 16. Comparison of 1-D (a) and 2-D (b) reflectometry.

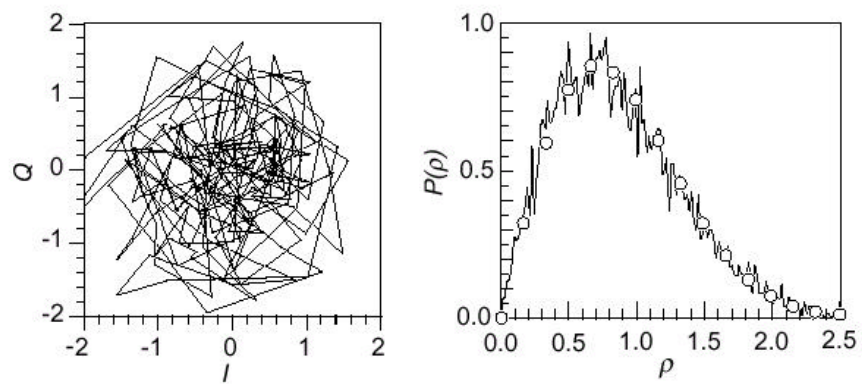


Figure 17. In-phase (I) and quadrature (Q) components of a TFTR reflectometer signal in a 200 s window (left), and probability density distribution of the signal amplitude $r = \sqrt{I^2 + Q^2}$ (right), open circles are the Rayleigh distribution $[2r \exp(-r^2)]$.

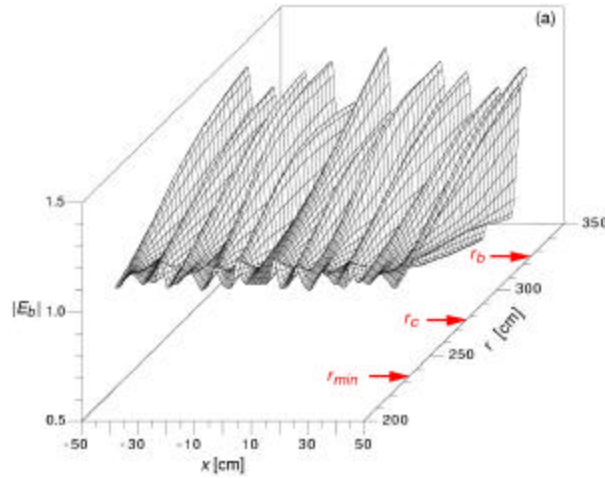


Figure 18. Isometric surface plot of the normalized field amplitude of the reflected wave, from the numerical simulations in Ref. 7. The plasma boundary is labeled r_b , r_c is the cutoff location, and r_{min} is the location of the “virtual cutoff”, which exhibits a minimum distortion of the field amplitude.

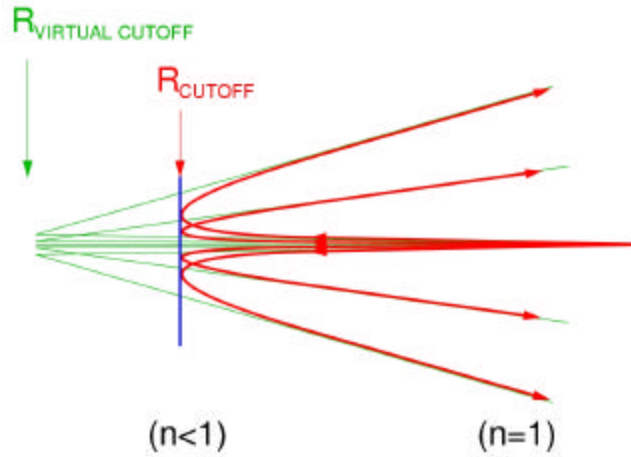


Figure 19. Schematic representation of beam trajectories in the vicinity of the cutoff layer. Return rays appear to an observer at the plasma boundary to have undergone specular reflection at the virtual cutoff location.

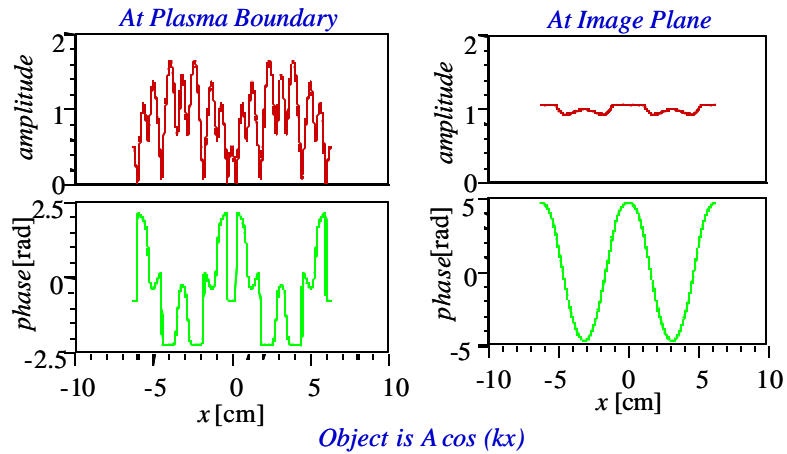


Figure 20. Results from a comparison study between standard (left) and imaging (right) reflectometry.

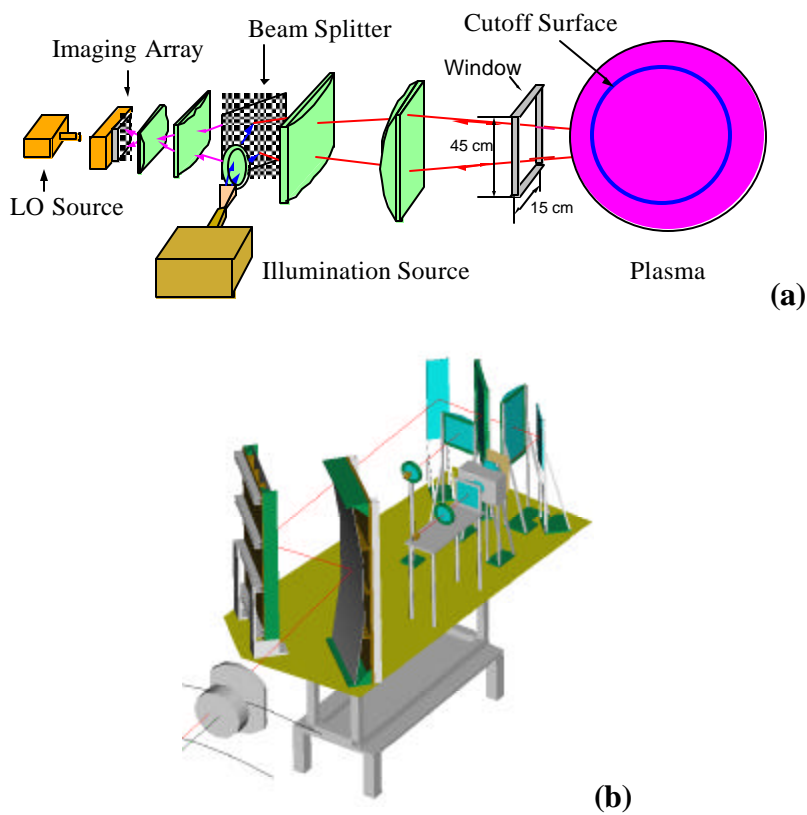


Figure 21. System configuration of an imaging reflectometry (a) and optical system layout of TEXTOR-94 MIR system (b).

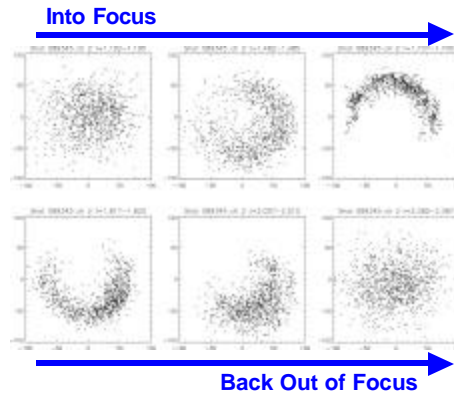


Figure 22. Complex field amplitude from the prototype TEXTOR-94 MIR system as the cutoff layer is swept through the focal plane of the imaging optics. Each frame represents a 3 ms time window.

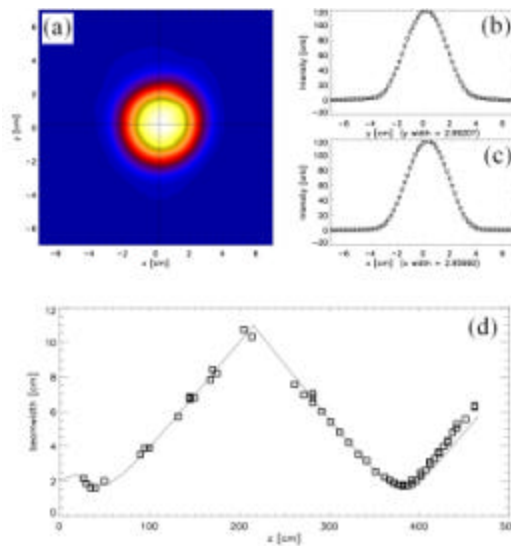


Figure 23. Gaussian beam patterns (a, b, and c) launched from a high performance horn and its propagation through high quality optics (d).

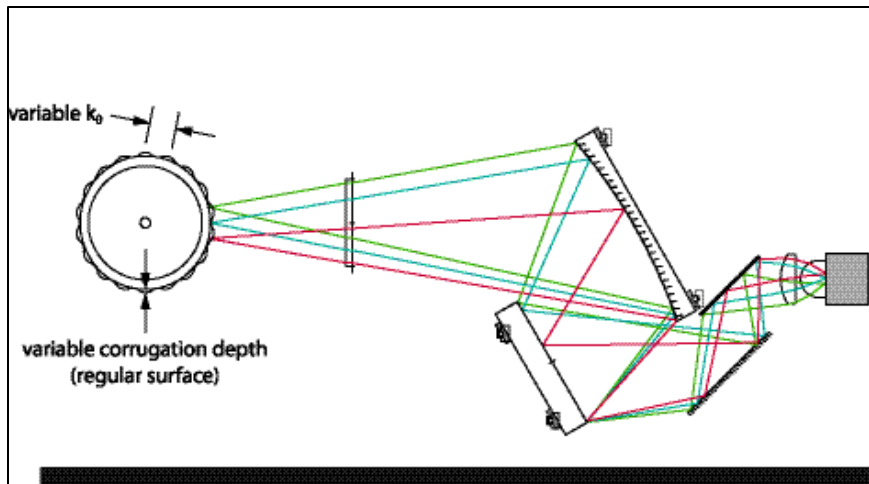


Figure 24. Laboratory setup for MIR system testing using a corrugated target mirror. Each target was tested using both the MIR configuration (above) and a standard 1-D configuration (not shown) consisting of a launched Gaussian beam and a receiving horn with no optics. As a reference, each surface was independently measured using a visible-laser interferometer (Leica “Laser Tracker”).

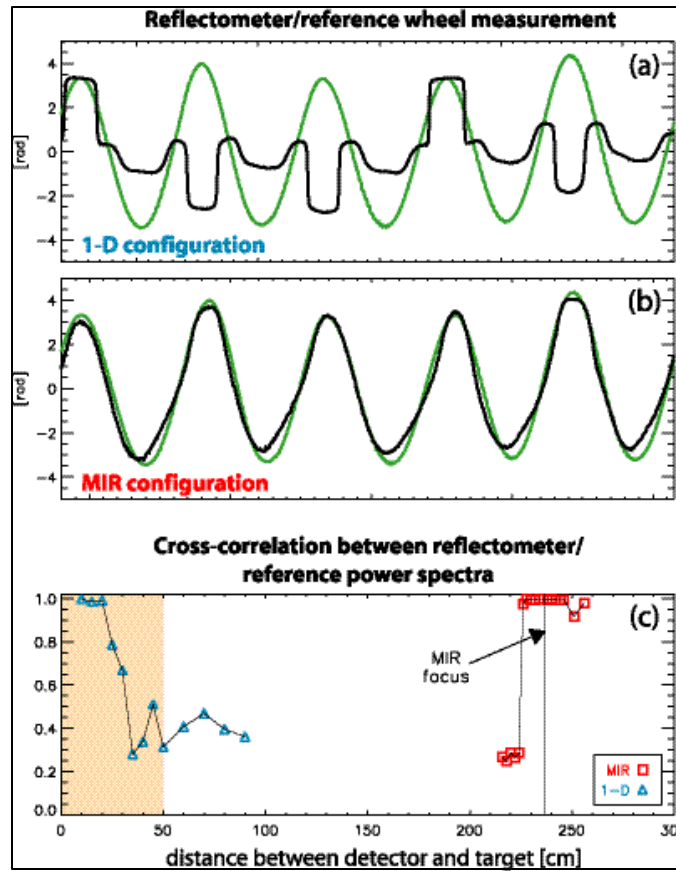


Figure 25. Comparison of 1-D and MIR reflectometer signals, using target reflector with k_{θ} of 1.25 cm^{-1} . Comparison of 1-D measurement (a) and MIR measurement (b) to reference measurement (green curve). 1-D measurement was taken at a distance of 30 cm and MIR measurement was taken at a distance of 235 cm. Plot (c) is the cross-correlation of the power spectra produced by the 1-D and MIR reflectometers, plotted as a function of d , the distance between the instrument and the target surface. The MIR focal plane is indicated by the vertical line at $d=237 \text{ cm}$. The region for $d < 50 \text{ cm}$ is shaded, representing the region inaccessible to diagnostics for core measurements in standard tokamaks.

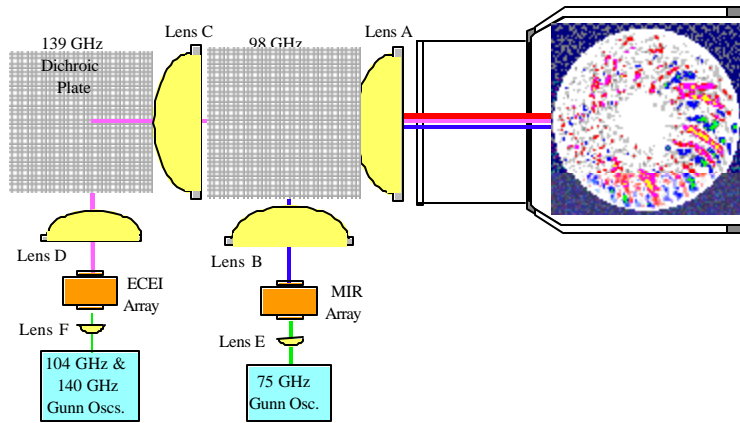


Figure 26. Combined 3 D ECEI and MIR system for simultaneous measurement of density and temperature fluctuations.

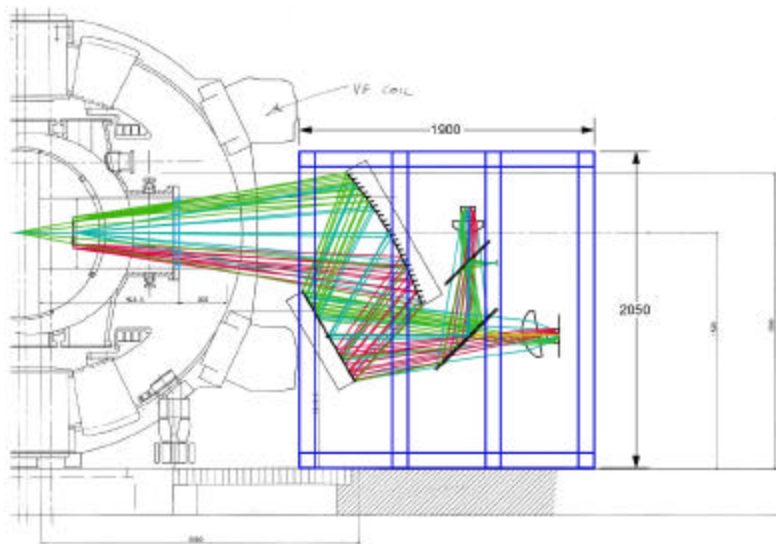


Figure 27. Layout of the combined ECEI/MIR system, showing the TEXTOR-94 cross-section, the optical components, and the diagnostic support framework.

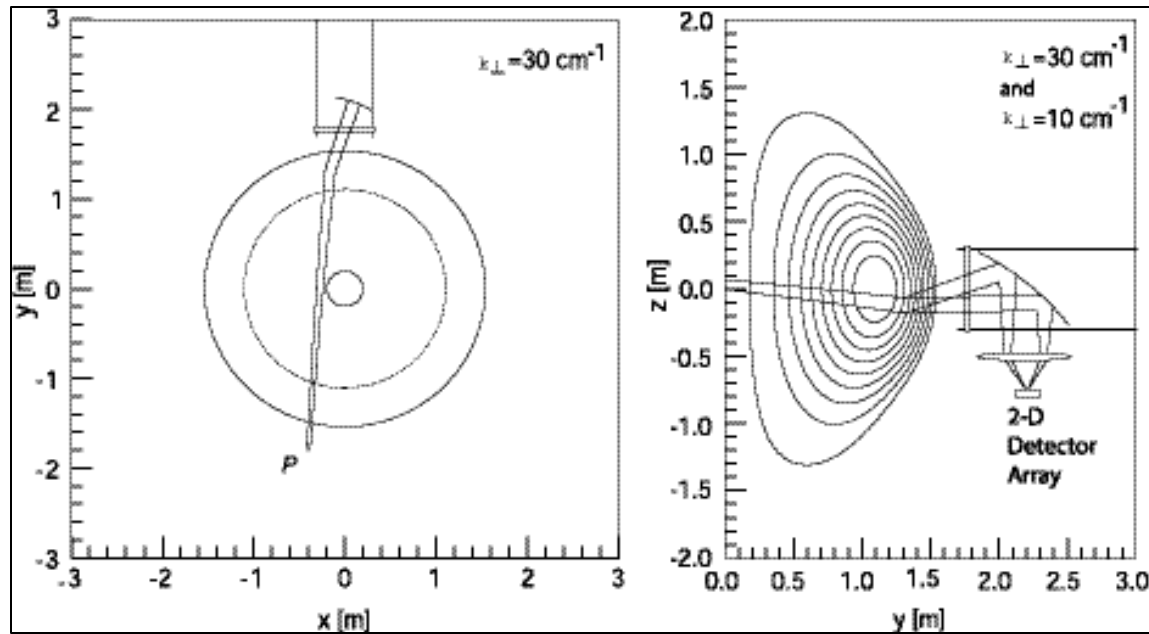


Figure 28. Equatorial (left) and poloidal (right) projections of a scattering geometry for the detection of poloidal fluctuations in NSTX with $k_{\perp}=30 \text{ cm}^{-1}$. The beam trajectories (from a ray tracing code [20]) are those of points with e^{-2} intensity. Scattered signals can be imaged on 2-D array to measure spatially resolved multi- \mathbf{k} spectras

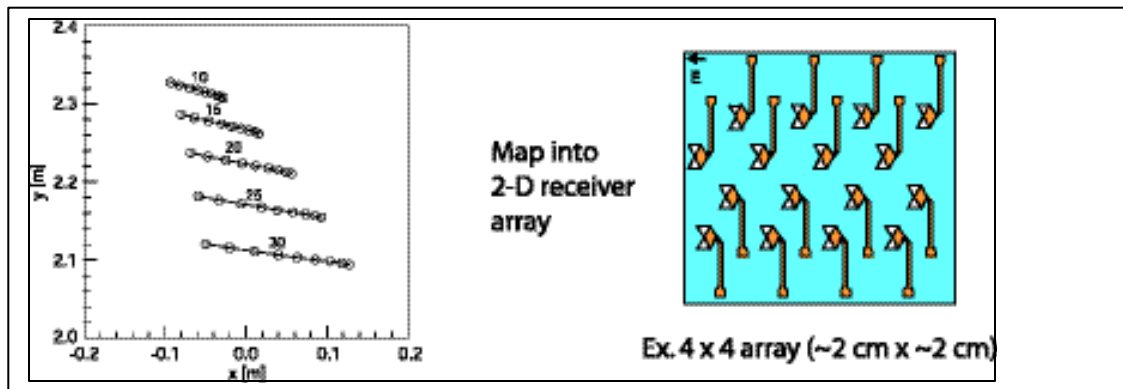


Figure 29. Position of scattered beams on the focal plane (label is the value of k_{\perp}); radius of circles is the waist of the scattered beam on the focal plane. Focal plane (40 cm x 40 cm) can be imaged on a small 2-D array.

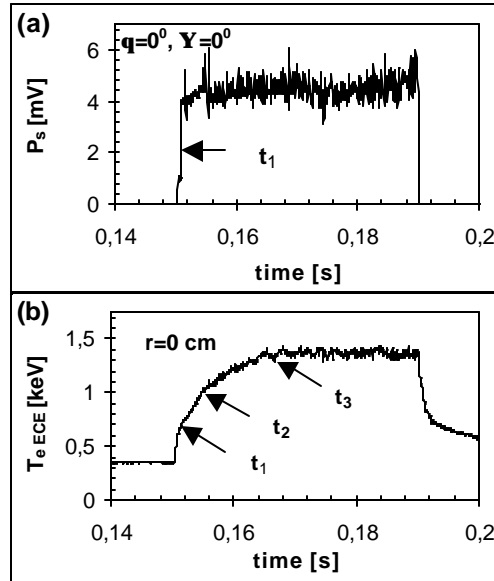


Figure 30. (a) X-mode signal of the central horn of the detection system. The ECRH pulse is applied from 150 to 190 ms. (b) Central electron temperature in the plasma as measured by ECE.

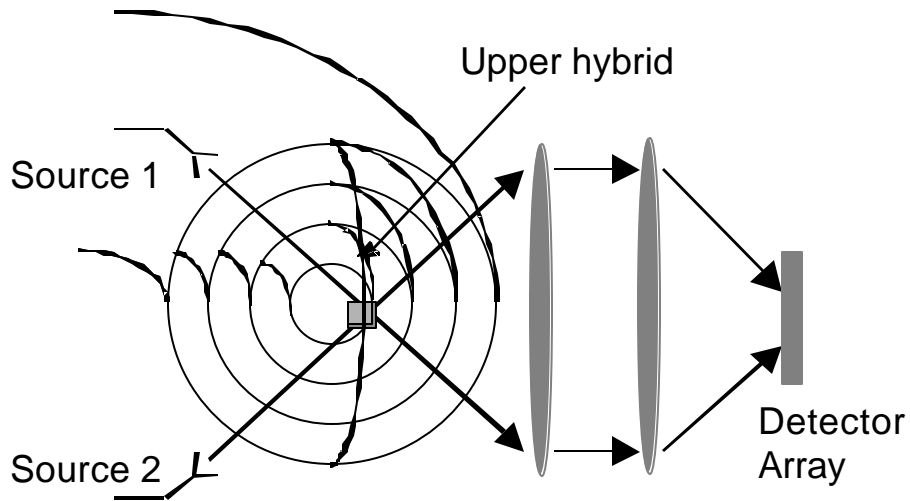


Figure 31. Schematic drawing of the proposed cross-polarization scattering imaging system.

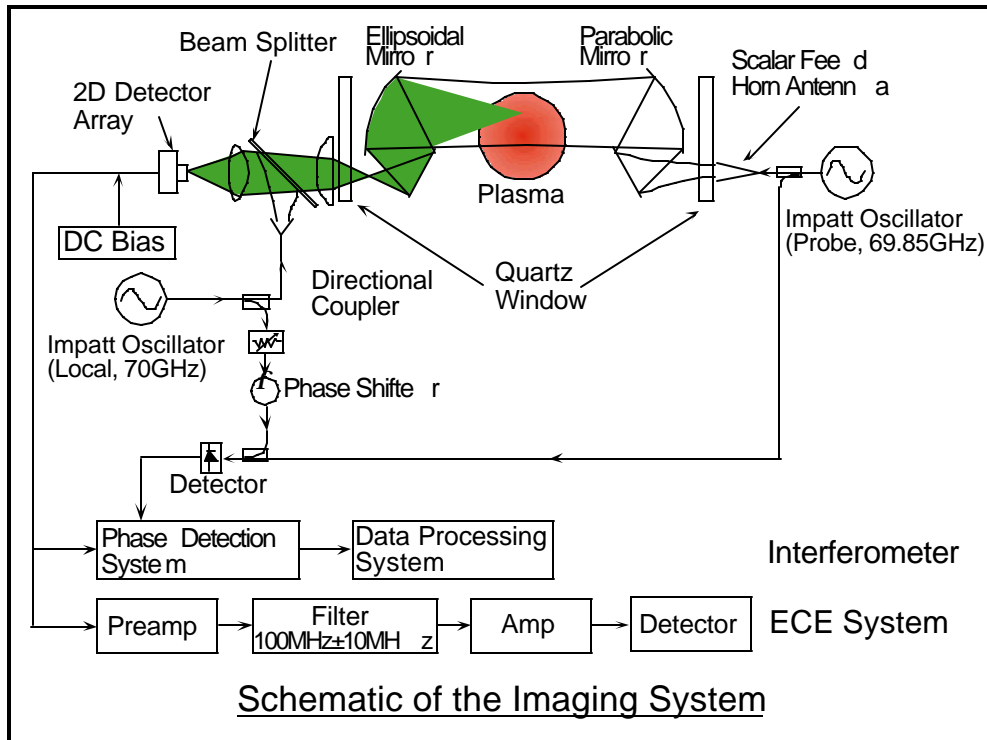


Figure 32. Schematic of the 2D imaging system on GAMMA 10.

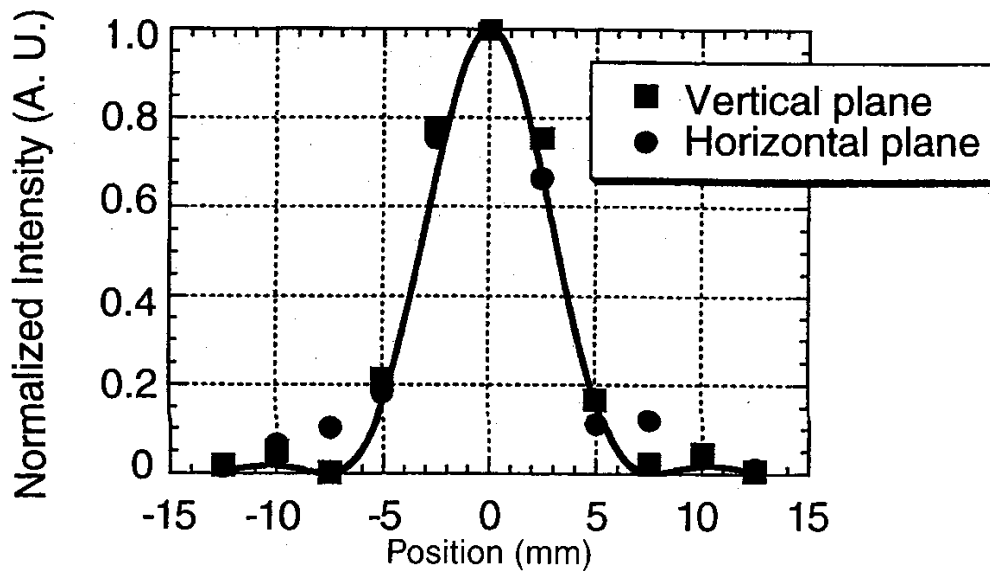


Figure 33. The Airy patterns in the horizontal and vertical planes.

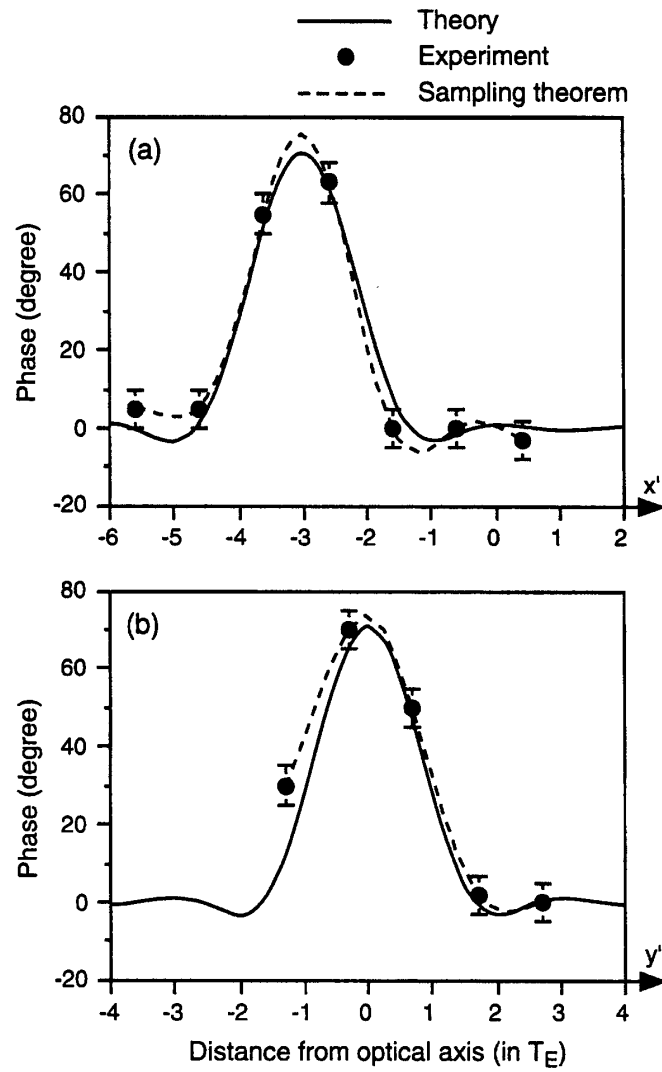


Figure 34. The 2D image of a Teflon plate of 10.1 mm x 10.1 mm size and 1.5 mm thickness in horizontal and vertical directions.

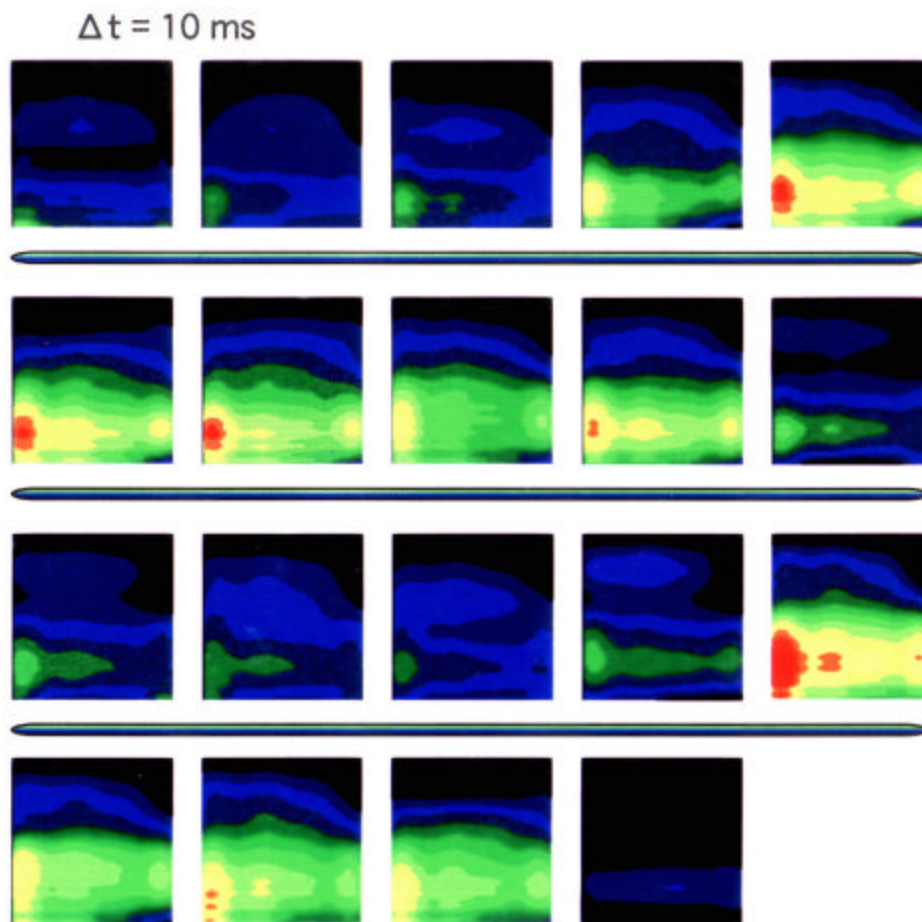


Figure 35. The changes of the GAMMA10 density profiles during the application of the ECRH. The starting time is 50 ms. The red color corresponds to $3.2 \times 10^{12} \text{ cm}^{-2}$.

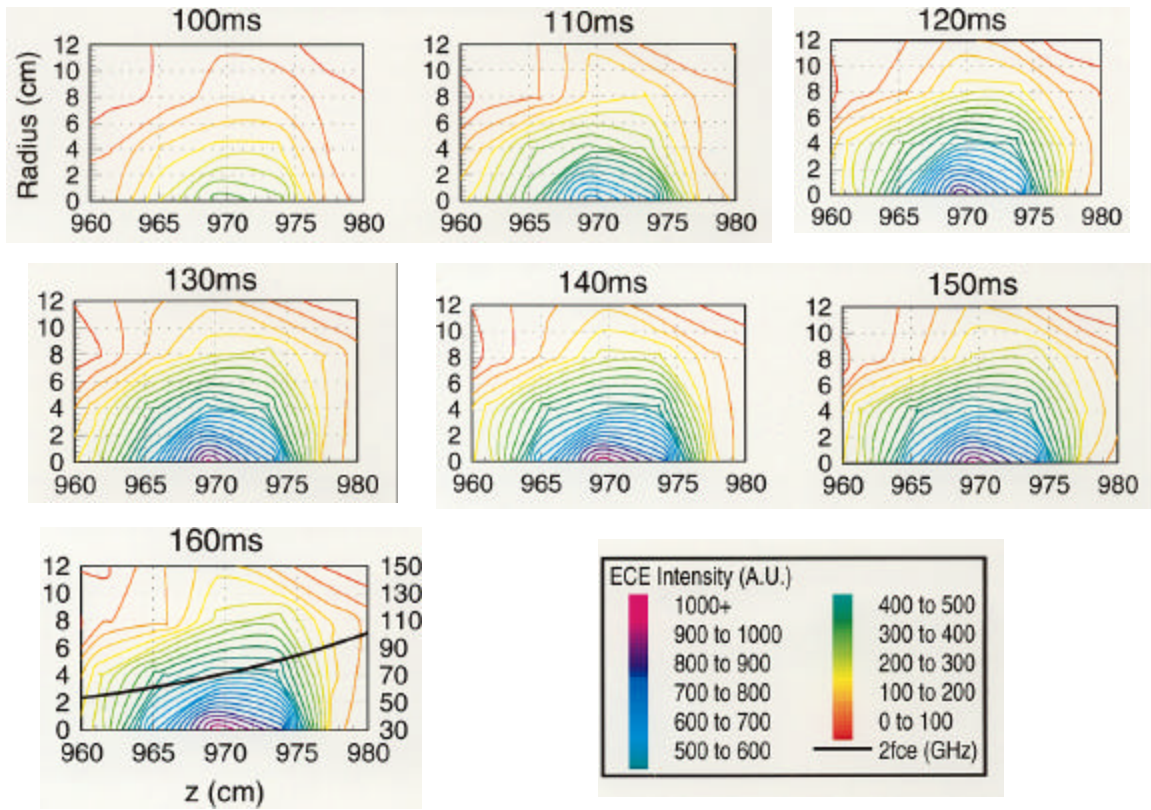


Figure 36. The time evolution of the ECE profile: the contour plot of the 2D ECE intensity.

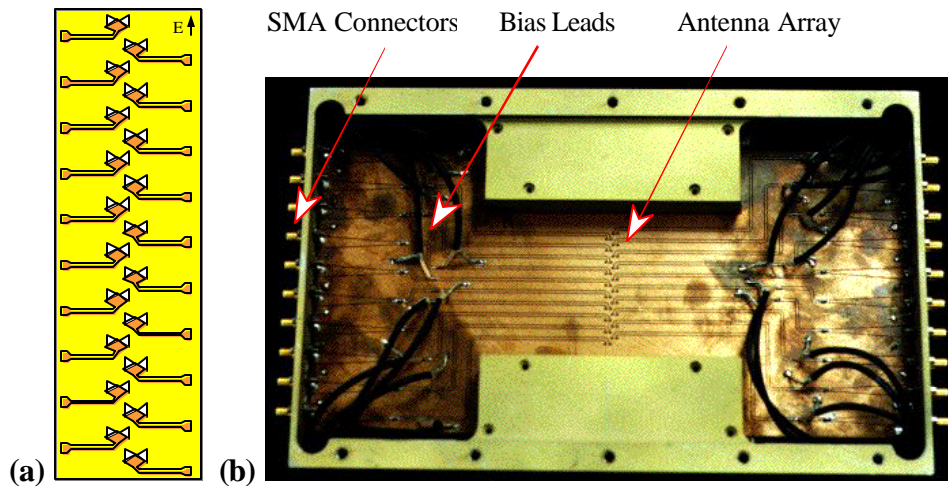


Figure 37. (a). Sample layout of an ECEI array, and (b) photograph of a hybrid imaging array mounted in an RF shielded enclosure.

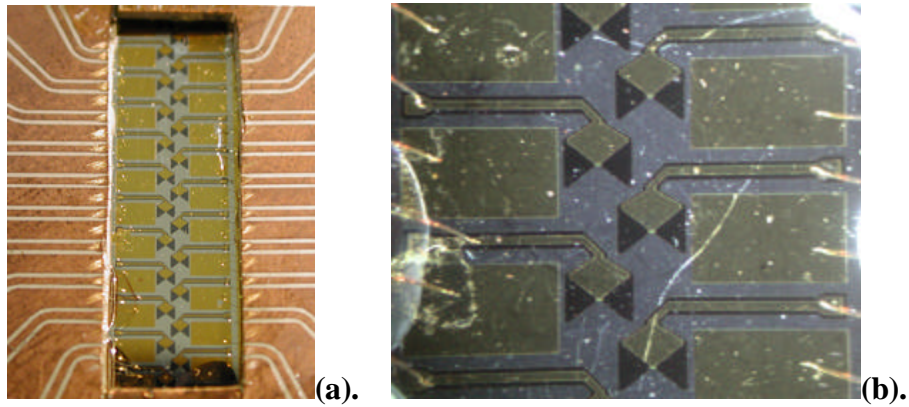


Figure 38. Photographs of a monolithic slot bow tie antenna/mixer array assembled with printed circuit board (a) and close-up view showing the wire bonding (b).

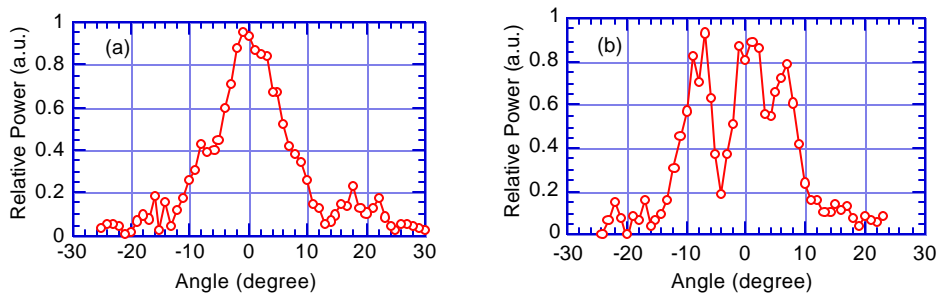


Figure 39. E-Plane (a) and H-Plane (b) antenna patterns of the monolithic SBT array measured at 100 GHz.

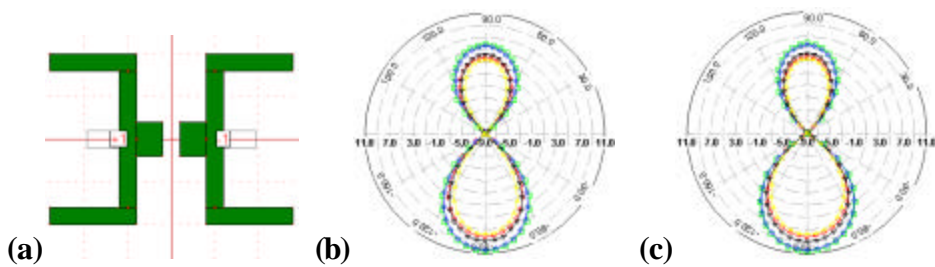


Figure 40. (a) The 85 GHz dual dipole antenna layout, and the corresponding (b) E-plane, and (c) H-plane antenna pattern simulation results at frequencies from 75 to 95 GHz.

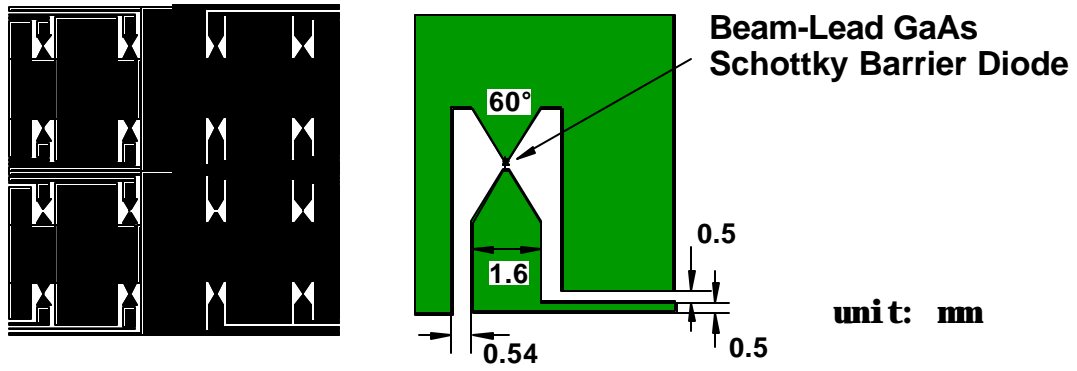


Figure 41. Schematic of the 2-D imaging array.

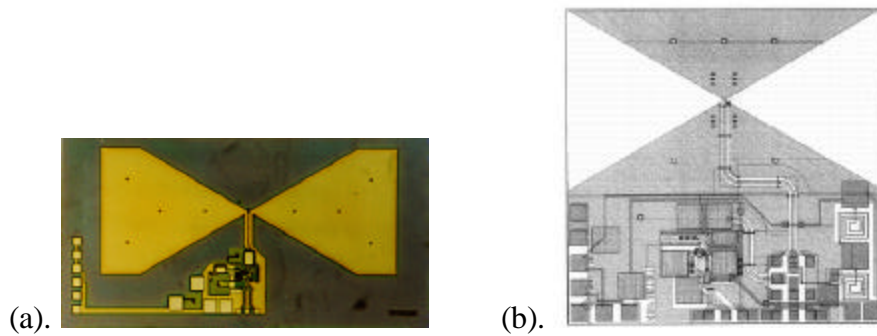


Figure 42. Mask patterns of the monolithic detectors integrated with bow tie antennas, Schottky diodes, and HBT amplifiers.

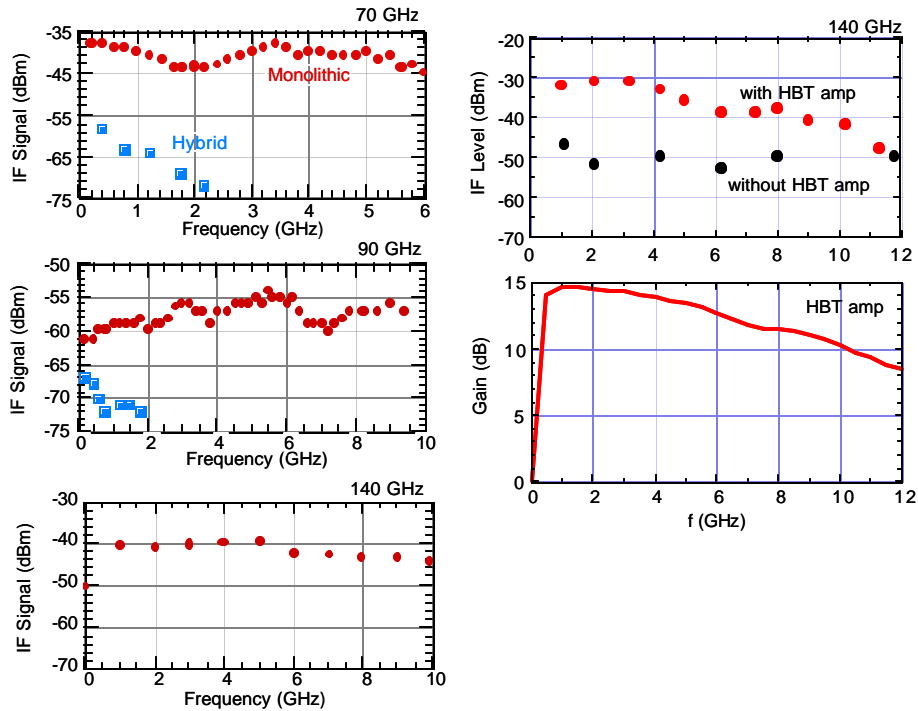


Figure 43. Heterodyne signal intensity as a function of IF frequency measured with a spectrum analyzer.

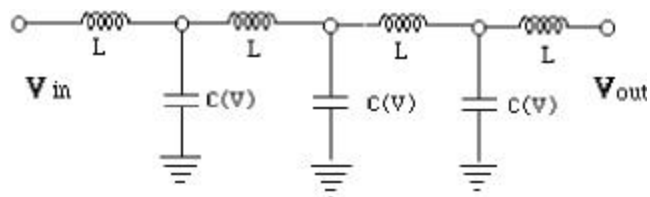


Figure 44. Transmission line equivalent circuit model of a varactor diode loaded Coplanar Waveguide (CPW)

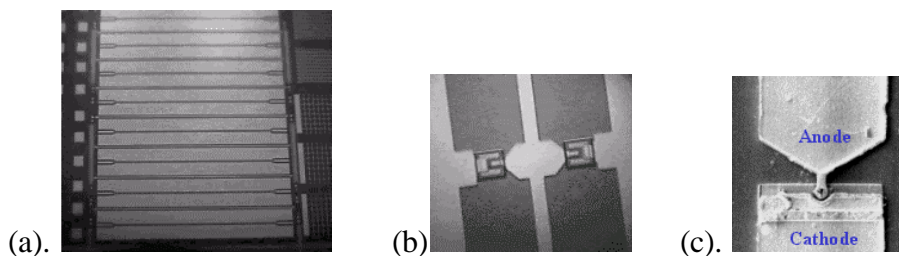


Figure 45. (a). Eight of the 80 section NDLs (b). Single NDL section (c). Schottky varactor diode

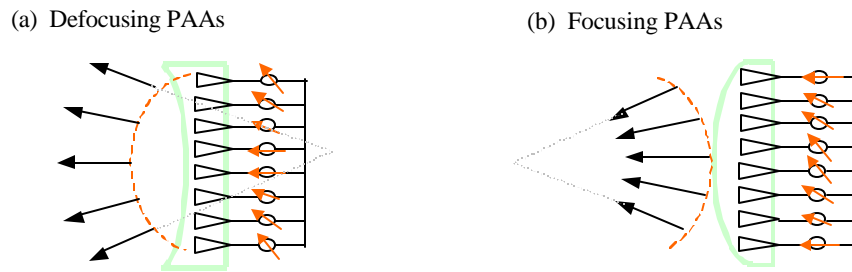


Figure 46. (a) Convex wave fronts generated by defocusing PAAs (b) Concave wave fronts generated by focusing PAAs.

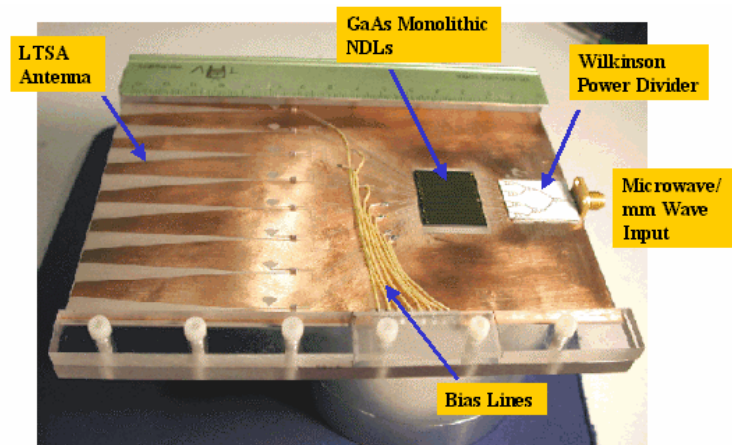


Figure 47. A proof-of-principle 1x8 PAA employing monolithically fabricated NDLs. This exhibited $\pm 15^\circ$ beam steering range in the 6-18 GHz region.

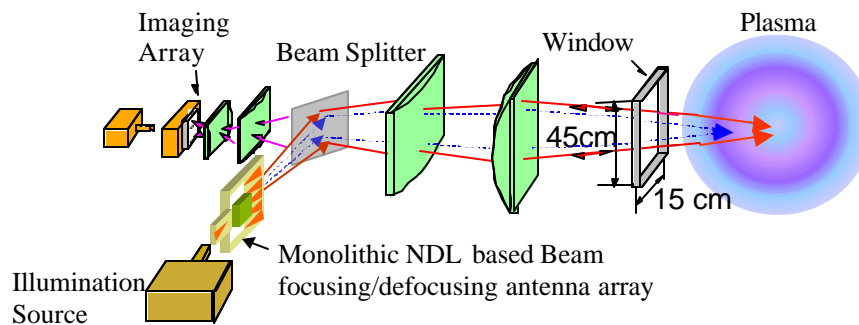


Figure 48. Block diagram of MIR system integrated with the phased antenna array as the illumination source.

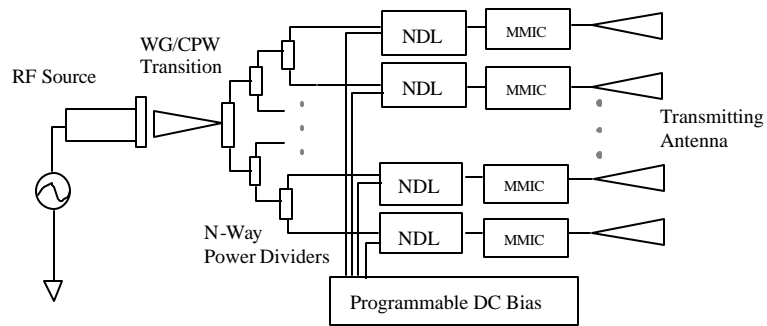


Figure 49. Block diagram of the NDL-based beam focusing/defocusing array

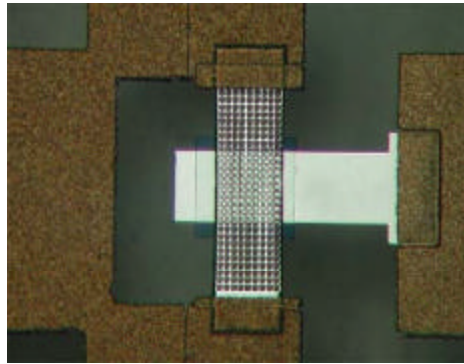


Figure 50. Single Air Bridge Structure MEMS Switch.

External Distribution

Plasma Research Laboratory, Australian National University, Australia
Professor I.R. Jones, Flinders University, Australia
Professor João Canalle, Instituto de Fisica DEQ/IF - UERJ, Brazil
Mr. Gerson O. Ludwig, Instituto Nacional de Pesquisas, Brazil
Dr. P.H. Sakanaka, Instituto Fisica, Brazil
The Librarian, Culham Laboratory, England
Library, R61, Rutherford Appleton Laboratory, England
Mrs. S.A. Hutchinson, JET Library, England
Professor M.N. Bussac, Ecole Polytechnique, France
Librarian, Max-Planck-Institut für Plasmaphysik, Germany
Jolan Moldvai, Reports Library, MTA KFKI-ATKI, Hungary
Dr. P. Kaw, Institute for Plasma Research, India
Ms. P.J. Pathak, Librarian, Institute for Plasma Research, India
Ms. Clelia De Palo, Associazione EURATOM-ENEA, Italy
Dr. G. Grosso, Instituto di Fisica del Plasma, Italy
Librarian, Naka Fusion Research Establishment, JAERI, Japan
Library, Plasma Physics Laboratory, Kyoto University, Japan
Research Information Center, National Institute for Fusion Science, Japan
Dr. O. Mitarai, Kyushu Tokai University, Japan
Library, Academia Sinica, Institute of Plasma Physics, People's Republic of China
Shih-Tung Tsai, Institute of Physics, Chinese Academy of Sciences, People's Republic of China
Dr. S. Mirnov, TRINITI, Troitsk, Russian Federation, Russia
Dr. V.S. Strelkov, Kurchatov Institute, Russian Federation, Russia
Professor Peter Lukac, Katedra Fyziky Plazmy MFF UK, Mlynska dolina F-2, Komenskeho
Univerzita, SK-842 15 Bratislava, Slovakia
Dr. G.S. Lee, Korea Basic Science Institute, South Korea
Mr. Dennis Bruggink, Fusion Library, University of Wisconsin, USA
Institute for Plasma Research, University of Maryland, USA
Librarian, Fusion Energy Division, Oak Ridge National Laboratory, USA
Librarian, Institute of Fusion Studies, University of Texas, USA
Librarian, Magnetic Fusion Program, Lawrence Livermore National Laboratory, USA
Library, General Atomics, USA
Plasma Physics Group, Fusion Energy Research Program, University of California at San
Diego, USA
Plasma Physics Library, Columbia University, USA
Alkesh Punjabi, Center for Fusion Research and Training, Hampton University, USA
Dr. W.M. Stacey, Fusion Research Center, Georgia Institute of Technology, USA
Dr. John Willis, U.S. Department of Energy, Office of Fusion Energy Sciences, USA
Mr. Paul H. Wright, Indianapolis, Indiana, USA

The Princeton Plasma Physics Laboratory is operated
by Princeton University under contract
with the U.S. Department of Energy.

Information Services
Princeton Plasma Physics Laboratory
P.O. Box 451
Princeton, NJ 08543

Phone: 609-243-2750
Fax: 609-243-2751
e-mail: pppl_info@pppl.gov
Internet Address: <http://www.pppl.gov>